Surface Wave Effects on High-Frequency Currents over a Shelf Edge Bank

H. W. WIJESEKERA, D. W. WANG, W. J. TEAGUE, E. JAROSZ, AND W. E. ROGERS

Naval Research Laboratory, Stennis Space Center, Mississippi

D. B. FRIBANCE

Coastal Carolina University, Conway, South Carolina

J. N. MOUM

Oregon State University, Corvallis, Oregon

(Manuscript received 5 October 2012, in final form 9 April 2013)

ABSTRACT

Several acoustic Doppler current profilers and vertical strings of temperature, conductivity, and pressure sensors, deployed on and around the East Flower Garden Bank (EFGB), were used to examine surface wave effects on high-frequency flows over the bank and to quantify spatial and temporal characteristic of these high-frequency flows. The EFGB, about 5-km wide and 10-km long, is located about 180-km southeast of Galveston, Texas, and consists of steep slopes on southern and eastern sides that rise from water depths over 100 m to within 20 m of the surface. Three-dimensional flows with frequencies ranging from 0.2 to 2 cycles per hour (cph) were observed in the mixed layer when wind speed and Stokes drift at the surface were large. These motions were stronger over the bank than outside the perimeter. The squared vertical velocity w^2 was strongest near the surface and decayed exponentially with depth, and the e-folding length of w^2 was 2 times larger than that of Stokes drift. The 2-h-averaged w^2 in the mixed layer, scaled by the squared friction velocity, was largest when the turbulent Langmuir number was less than unity and the mixed layer was shallow. It is suggested that Langmuir circulation is responsible for the generation of vertical flows in the mixed layer, and that the increase in kinetic energy is due to an enhancement of Stokes drift by wave focusing. The lack of agreement with open-ocean Langmuir scaling arguments is likely due to the enhanced kinetic energy by wave focusing.

1. Introduction

The oceanic surface layer is controlled by momentum and buoyancy fluxes near the surface and by entrainment fluxes at the base of the mixed layer. These fluxes generate a wide range of physical processes between the air–sea interface and thermocline, and play a vital role in climate variability, biological productivity, and marine pollution. In the highly unstable boundary layer, buoyancy dominates the production of turbulent kinetic energy (TKE) (e.g., Shay and Gregg 1986; Brubaker 1987; Lombardo and Gregg 1989). The production of TKE driven by surface cooling initially modifies the vertical velocity component and is then transferred by turbulent pressure forces into horizontal velocity components, thus generating coherent flows in geophysical boundary layers (see, e.g., Lumley and Panofsky 1964; Thorpe 2005). When the surface buoyancy flux is small and the boundary layer is near neutral, the production of TKE is dominated by shear production driven by surface wind stress (Dillon et al. 1981; Soloviev et al. 1988). Shear production modifies horizontal velocity fluctuations, especially in the downwind direction before transferring energy to the crosswind and vertical energy components via turbulent pressure fluctuations. These ideas have been used in turbulent closure schemes in the oceanic mixed layer (e.g., Mellor and Yamada 1982).

However, transfer of momentum and buoyancy at the air–sea interface is complicated by the presence of surface waves. Surface waves boost the vertical transport of surface fluxes through (i) enhancement of TKE dissipation by breaking and (ii) generation of production-scale

Corresponding author address: Hemantha W. Wijesekera, Naval Research Laboratory, Stennis Space Center, MS 39529.
E-mail: hemantha.wijesekera@nrlssc.navy.mil

DOI: 10.1175/JPO-D-12-0197.1

coherent structures in the mixed layer via wave–mean flow interactions. Several investigators (Agrawal et al. 1992; Anis and Moum 1995; Drennan et al. 1996; Melville 1996; Terray et al. 1996; Soloviev and Lukas 2003) report that the dissipation rate of TKE in the wave boundary layer is up to an order of magnitude larger than the predictions from wall boundary layer scaling. The enhanced TKE dissipation rate by wave breaking is an important factor for momentum, heat, and gas transfer rates at the air–sea interface.

As a response to the wind over the ocean, roll vortices are formed roughly parallel to the wind direction. These circulation patterns can be recognized by the lines of convergence at the surface, as noted by Langmuir (1938), and they are referred as ''Langmuir cells.'' The orientation of these Langmuir cells is roughly opposed to the orientation of wind-/shear-driven turbulent eddies in the mixed layer. Craik and Leibovich (1976) describe a plausible theory for the generation of roll vortices. The Craik–Leibovich mechanism requires interaction between surface waves and wind-driven shear flows to generate a forcing function governed by the wave-induced Stokes drift and vertical shear of mean currents. In Langmuir turbulence, the Stokes production term generates TKE in both crosswind and vertical directions. Detailed discussions of theory and relevant references are in Leibovich (1983) and Thorpe (2004).

Several investigators observed convergence zones on the surface layer and the associated crosswind and vertical velocities in surface convergence zones (Weller and Price 1988; Smith et al. 1987; Pollard and Thomas 1989; Zedel and Farmer 1991; Smith 1992, 1998; Plueddemann et al. 1996). Weller and Price (1988) report three-dimensional structure in mixed layer velocity and narrow regions of downwelling flow within the mixed layer, in coincidence with bands of convergent surface flow. They further report that the downwelling flow in the middle of the mixed layer was up to 0.2 m s^{-1}, and that the downwind, downwelling flow had a jetlike structure. Coherent vortices in the mixed layer have been studied using Doppler sonar techniques (e.g., Zedel and Farmer 1991; Plueddemann et al. 1996; Smith 1992, 1998) and these investigators report the consistency of wind/wave forcing of Langmuir circulation. In the existing literature on Langmuir circulation studies, the majority of the observations is from deep water environments and there are only a few references related to shallow-water environments (e.g., Hunter and Hill 1980; Marmorino et al. 2005; Gargett and Wells 2007). In a shallow-water environment, the physical setup is different since top and bottom boundary layers can merge under wind and buoyancy forcing, and thus bottom frictional effects can become a significant factor in mixed layer dynamics. Gargett and Wells (2007) report that Langmuir circulation plays an important role in sediment transport in the shallow-water environment.

There are numerous numerical-modeling studies, mainly large-eddy simulations (LESs), to examine, quantify, and scale Langmuir turbulence in the oceanic mixed layer (Skyllingstad and Denbo 1995; McWilliams et al. 1997; Skyllingstad et al. 1999; Li et al. 2005; Harcourt and D'Asaro, 2008; Grant and Belcher 2009). The papers cited here are just a few references out of many in the literature on this subject. In the majority of these models, Langmuir circulation is simulated by specifying Craik and Leibovich (1976) vortex-force parameters while specifying a Stokes drift corresponding to a monochromatic surface wave field. These studies describe the formation of Langmuir circulation, scaling of Langmuir turbulence, and the distinction among convection, shear-driven turbulence, and Langmuir flows in the upper ocean.

However, there are still unresolved issues such as quantitative understanding of the three-dimensional structure of Langmuir circulation and its interaction with convective- and shear-driven mixing and with internal waves in the thermocline, and scaling laws for Langmuir turbulence. The main objectives of this study are to examine surface wave effects on high-frequency flows over the East Flower Garden Bank (EFGB), to quantify spatial and temporal characteristics of these high-frequency flows, and to examine the scaling laws of vertical velocity based on Langmuir circulation theory. In this paper, we describe measurements of high-frequency currents over the EFGB. The bank is located at the edge of the Texas–Louisiana continental shelf and rises from depths of 100–150 m to about 20-m below the surface. When compared with previous observations from shallow (e.g., Gargett and Wells 2007) and deep water (e.g., Smith 1998), our measurements represent both shallow- and deep-water conditions. The vertical velocity fluctuations described here show strong correlations with winds and surface wave properties. We suspect that these velocity fluctuations are a manifestation of Stokes drift–induced wave–current interactions such as Langmuir circulations during wind events. Here, we examine high-frequency velocity fluctuations including temporal, lateral, and vertical distributions, and characteristic vertical length scales for wide ranges of wind speeds and Stokes drifts. The paper is organized as follows. Section 2 describes platforms and measurements. Section 3 describes observations of winds, surface wave statistics, and background currents and hydrography. High-frequency velocity fluctuations and scaling of vertical velocity are described in section 4. A discussion is given in section 5. Finally, major findings are summarized in section 6.

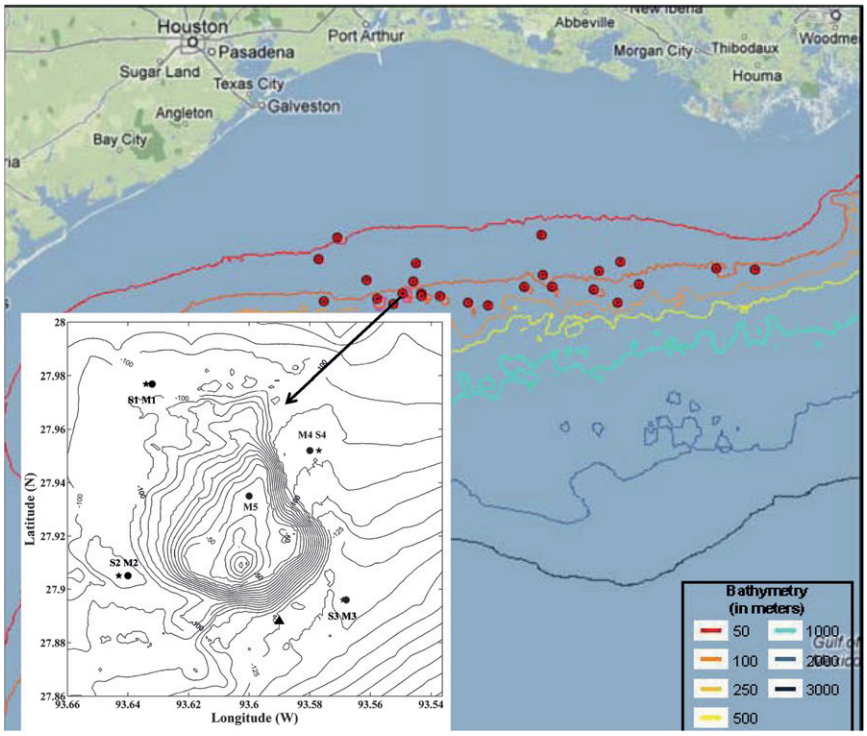

FIG. 1. Location of the Flower Garden Banks National Marine Sanctuary. Red circles, representing salt domes or banks, are shown with selected bathymetric contours. The black and white inset illustrates bathymetric contours of EGFB and the locations of bottom-mounted ADCP (M1–M5; filled circles) and string (S1–S4; filled stars) moorings. The contour interval is 5 m. The filled triangle denotes NDBC buoy 42047.

2. Platforms and measurements

Closely spaced observations of velocity (i.e., u, v, w), temperature T, conductivity C, and pressure P were collected between December 2010 and December 2011 over the EFGB as part of projects sponsored by the Naval Research Laboratory (NRL) [Mixing Over Rough Topography (MORT)] and by the Bureau of Ocean Energy Management (BOEM) [Currents over Banks (COB)]. The year-long observational program consists of two 6-month mooring deployments (from December 2010 to June 2011 and from June to December 2011), and a 2-week intensive experiment from 26 May to 14 June 2011. A detailed discussion of instrumentation, data collection, sampling methods, and data processing is in Teague et al. (2013, hereafter TG) and therefore we just describe a subset of the data, relevant to this study, which is mainly from measurements made during the second half of the experiment (June–December 2011).

Currents and hydrographic fields were collected from five trawl-resistant bottom-mounted ADCP moorings (M1–M5), referred to as ''Barnys'' because of their barnacle-shaped dome (Perkins et al. 2000), and four subsurface string moorings (S1–S4), equipped with temperature, conductivity, and pressure (TCP) sensors. Bathymetry and locations of moorings at the EFGB are shown in Fig. 1. M1–M4 and S1–S4 were deployed at the four corners of the bank at water depths of 98, 105, 127, and 106 m, respectively, and M5 was deployed at a water of depth of 47 m, about 3-km north of the bank peak (about 20-m depth) (Fig. 1). The separations between Barnys and associated string moorings were about 200 m. The moorings were equipped with Teledyne RD Instruments Workhorse ADCPs operating at 600 (M5) and 300 kHz (M1–M4) with four transducers each with an incidence angle of 20°. ADCPs recorded near-full water column current profiles every 15 min (an ensemble average of 120 realizations). The ADCPs at M1, M2, M4, and M5 had 2-m vertical resolution and at M3 had 4-m vertical resolution. Shallowest ADCP bins at M1, M2, M3, M4, and M5 were 7.5-, 10.4-, 16.4-, 11.5-, and 5.5-m below the mean water line, respectively, while the deepest bins were off the bottom by 6.5, 4.6, 11, 4.5, and 3.5 m, respectively. The standard deviations for 15-min-averaged currents were less than 0.5% of the water velocity at the five mooring sites. Because moorings are

bottom mounted, the platform motion is not a factor for velocity measurements. Apart from water column velocities at M5, surface wave parameters such as wave height spectra and directional wave spectra were collected from the ADCP (Strong et al. 2000). The spectral distribution of wave energy $E(f, \theta)$ in frequency f and direction θ was provided by a bottom-mounted upward-looking ADCP (600 kHz) based on the Teledyne RD Instrument's Wave Array Technique. It treats the ADCP depth cell bins as an array of independent sensors for acquiring wave orbital velocities. The frequency–direction spectrum $E(f, \theta)$ is then derived using an array-processing algorithm for velocities acquired every 2 h for 5 min at a 2-Hz sampling rate. Three Barnys, at M2, M4, and M5, were also equipped with high-resolution pressure sensors (Ppods) developed by Moum and Nash (2008). The other two Barnys (M1, M3) contained SeaBird Electronics wave/tide gauges. The sampling rates of the Ppods were 1 Hz and the resolutions were about 0.14 mm or 1 Pa ($1\,\text{Pa} = 1\,\text{N m}^{-2}$).

Four TCP string moorings were deployed at M1–M4 during the first half of the deployment and three were redeployed at M2–M4 during the second half. Each string mooring contained 8–12 instruments that were approximately equally spaced between 7 and 12 m below the surface and 1-m above the bottom (TG). Some of the instruments recorded only T and C while others recorded T, C, and P. The large majority of the instruments were SeaBird Electronics MicroCats (SBE37). A limited number of Aqua Trolls that recorded T, C, and P were distributed on each of the string moorings. The MicroCats sampled every 6 min with accuracies of ±0.002°C and 3 μS cm^{-1}. The Aqua Trolls sampled every 12 min with lower accuracies of ±0.1°C and ±0.5% of the data magnitude plus 1 μS cm^{-1}. The conductivity sensors sometimes failed toward the ends of the records as a result of biofouling. We do not address processing and data quality issues here, because those topics are discussed in TG.

3. Winds, waves, and background currents

a. Wind field

Wind observations were collected hourly at the southern edge of the EFGB at the National Data Buoy Center (NDBC) station 42047 (Fig. 1) and at NDBC station 42046 located approximately 44 km west of the EFGB. Winds at 42046 were used when 42047 was out of service, which was about half of the year-long mooring period. Winds at two buoy locations were similar when they were available. No wave data were available at these sites. For this study wind measurements were from 42046. The buoy provides wind velocity ($\mathbf{U}_4$) at 4 m (i.e., Z_4) above the sea surface. The standard 10-m (i.e., Z_{10}) wind velocity ($\mathbf{U}_{10}$) was estimated iteratively by assuming that the near-surface atmospheric boundary layer was near neutral, where

$$\mathbf{U}_{10} \approx \mathbf{U}_4 + \mathbf{U}_* \kappa^{-1} \log(Z_{10}/Z_4), \tag{1a}$$

$$\mathbf{U}_* |\mathbf{U}_*| = \boldsymbol{\tau}/\rho_w, \tag{1b}$$

$$\boldsymbol{\tau} = \rho_a C_D \mathbf{U}_{10} |\mathbf{U}_{10}|, \quad \text{and} \tag{1c}$$

$$C_D = 10^{-4}(-0.016|\mathbf{U}_{10}|^2 + 0.967|\mathbf{U}_{10}| + 8.0558) \tag{1d}$$

(Hwang 2011). The friction velocity is $\mathbf{U}_*$, κ is the von Kármán constant (0.4), $\boldsymbol{\tau}$ is the wind stress at the sea surface, C_D is the drag coefficient, ρ_w is the density of seawater, and ρ_a is the density of air. Winds (U_{10}) for September–December were dominated by north–south changes in direction caused by passages of numerous fronts (Fig. 2a). Winds from May to August were primarily out of the southeast. Wind events with magnitudes larger than 8 m s^{-1} lasted from 1 to 6 days. Wind events associated with passages of cold fronts were limited to 1–3 days.

b. Surface waves and Stokes drift

The wave-induced Stokes drift profile for a random wave field $\mathbf{U}_S(z)$ is calculated as an ensemble average of wave components (Kenyon 1969), where

$$\mathbf{U}_S(z) = 4\pi \int_{f_{\min}}^{f_c} \int_0^{2\pi} f\mathbf{k} E(f,\theta) G(f,z)\, d\theta\, df. \tag{2}$$

The function $G(f,z)$ is expressed as $G(f,z) = \cosh[2k(H+z)][\sinh(2kH)]^{-1}$, where $k = |\mathbf{k}|$ is the wavenumber and $2\pi f = [gk\tanh(kH)]^{1/2}$. The water depth is H, the gravitational acceleration (9.81 m s^{-2}) is g, and the vertical depth coordinate (negative downward) from the mean sea surface is z. The ADCP wave measurement system provides $E(f,\theta)$ for a frequency band varying from minimum frequency $f_{\min}$ to cutoff frequency f_c. This frequency band varies with environmental conditions and during the experiment: $f_{\min} = 0.0098$ Hz and $f_c = 0.3535$ Hz. Stokes drift was computed at M5 where $H = 47$ m.

Figure 3 shows the ratio of surface Stokes drift $U_{S_0} = |\mathbf{U}_S(z=0)|$ to U_{10} as a function of U_{10}. In general, the direction of estimated Stokes drift follows the direction of the wind closely. Data presented in Fig. 3 are within 15° of the wind direction. The scatterplot shows

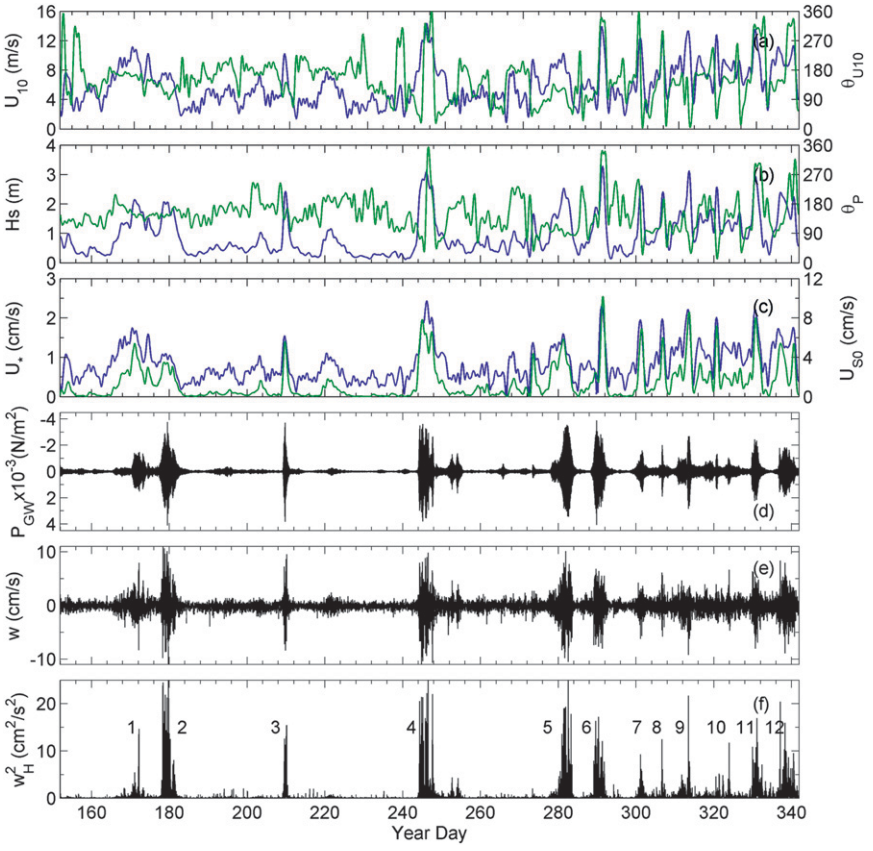

FIG. 2. Time series between 2 Jun (year day 152) and 8 Dec 2011 (year day 342). (a) Wind speed U_{10} (blue) and direction $\theta_{U_{10}}$ (green). (b) Surface wave height H_s (blue) and direction of wave corresponding to peak wave energy θ_P (green). (c) Frictional velocity U_* (blue) and Stokes drift velocity at surface U_{S_0} (green). (d) High-pass-filtered pressure (P_{GW}) at 47-m depth (bottom) from Ppod pressure sensor at M5; $P_{\mathrm{GW}}/1000$ is plotted. (e) Time series of 15-min-averaged vertical velocity at 5.5-m depth at M5, where water depth is 47 m. (f) Depth-averaged squared vertical velocity (w_H^2) at M5. Targeted wind events are numbered 1–12.

2-h estimates of the fractional Stokes drift U_{S_0}/U_{10} and the bin-averaged U_{S_0}/U_{10} over $1\,\mathrm{m\,s^{-1}}$ wind speed intervals with 95% confidence limits (circles with bars). As a reference, we also show U_{S_0}/U_{10}, derived from directional wave spectra and wind speeds from a nearby NDBC directional wave buoy (42019) located 170-km east of the EFGB (Fig. 3). Earle et al. (1999) showed that the directional wave distribution can be derived from: the directional Fourier series method, the Maximum Likelihood Method (MLM), and Maximum Entropy Method (MEM). In this study, the MLM was used to compute surface Stokes drift from the NDBC buoy data. We adapted this technique to be consistent with the Iterative Maximum Likelihood Method used for deriving ADCP directional wave spectra (Strong et al. 2000). We also computed surface Stokes drift from the Fourier method, and these results are plotted in Fig. 3. The fractional Stokes drift at M5 increases from about 0.1% to about 0.6% as wind speed increases from 5 to $15\,\mathrm{m\,s^{-1}}$. For winds greater than $10\,\mathrm{m\,s^{-1}}$, the ratio U_{S_0}/U_{10} at M5 is about 0.6, while that at the nearby NDBC buoy is about 0.7 for the MLM, and is about 0.8 for the Fourier method (Fig. 3). Note that the cutoff frequency of NDBC observation is 0.485 Hz.

Both wave measurement systems and wave-simulation models impose cutoff frequencies because of observational constraints and computational limitations. Therefore, wave spectral components below this cutoff frequency (i.e., f_c) are available for the estimate of Stokes drift [Eq. (2)]. Contributions from high-frequency spectral components can be approximated by assuming a spectral tail shape and directional spreading function for frequencies higher than f_c (Webb and Fox-Kemper 2011; Rascle et al. 2008; Belcher et al. 2012). The spectral tail with f^{-5} contributes 30% to the surface Stokes drift compared to the truncated spectrum with $f_c = 0.41$ Hz (Belcher et al. 2012). Rascle et al. (2008) show that the contribution can be about 0.4% of wind speed for

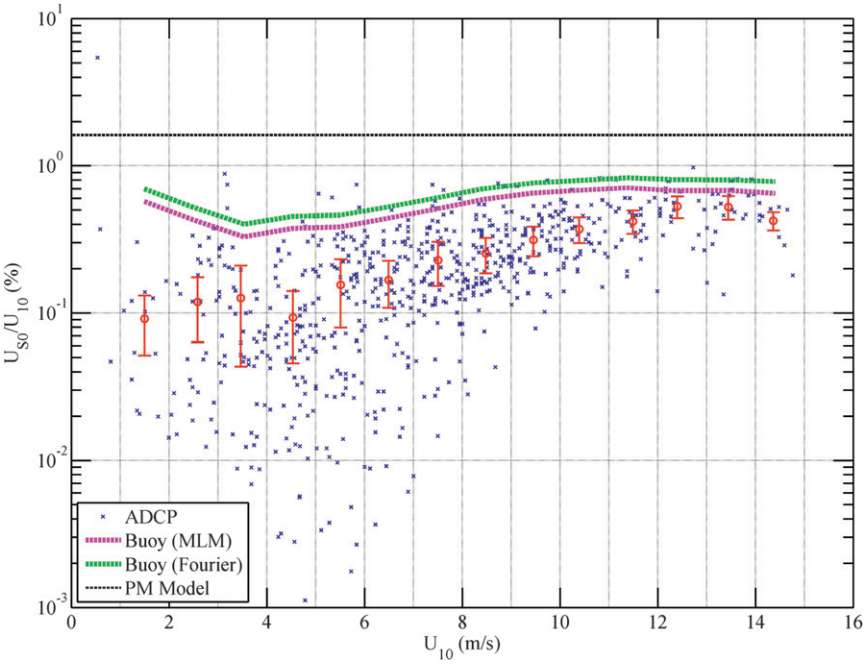

FIG. 3. Ratio of surface Stokes drift to wind speed, U_{S_0}/U_{10} vs U_{10}. Red circles are bin-averaged U_{S_0}/U_{10} for 1 m s^{-1} wind speed intervals. The error bars show one std dev. The magenta and green dashed lines represent bin-averaged results from NDBC buoy 42019 for all of 2011 based on directional spectra derived from the MLM and Fourier series methods, respectively. The black dashed line represents a value of 1.62% derived from the PM spectral model.

simulated wave spectra with f^{-5} slope and a constant directional spreading at frequencies beyond $f_c = 0.41$ Hz. The computation of the high-frequency contribution remains uncertain because of the lack of information about the high-frequency directional wave spectrum.

It is noted that Stokes drift resulting from shorter waves penetrate into a very shallow depth near the ocean surface. While short-wave breaking in a shallow layer is important for mixing near the surface (e.g., McWilliams et al. 1997), the contribution of high-frequency (short) wave forcing to Langmuir turbulence is not clear (Belcher et al. 2012). Therefore, in the following analysis, we limit our computation of Stokes drift to the imposed cutoff frequency similar to Kukulka et al. (2011). A detailed discussion of cutoff frequency effects on the Stokes drift estimate is beyond the scope of this study.

As illustrated in Fig. 3, the ratio U_{S_0}/U_{10} is a constant (= 0.0162) for the Pierson and Moskowitz (1964, hereafter PM) spectrum (Li and Garrett 1993; Webb and Fox-Kemper 2011). The PM spectrum represents a fully developed and unidirectional wave field. However, the ratio U_{S_0}/U_{10} is shown to be small relative to the PM spectral model and to vary with sea state development for spectral models of developing seas (Webb and Fox-Kemper 2011; Harcourt and D'Asaro 2008).

Time series of significant wave height (i.e., H_s), direction (i.e., θ_p) of dominant waves, and magnitude of Stokes drift at the surface (i.e., U_{S_0}), derived from ADCP wave measurements are shown in Figs. 2b and c. During wind events, wave height was about 3 m over the bank and the dominant wave period was about 8 s. Stokes drift was about 4–8 cm s^{-1}, which was a factor of 2–4 times larger than the friction velocity induced by surface winds (Figs. 2a–c). In most cases, the dominant surface waves propagated in the direction of the wind. Surface wave–produced pressure at the bottom (Fig. 2d) was measured by the Ppod in the M5 Barny mooring (47-m depth). Surface waves with a dominant wave period of 8 s, from bottom-pressure measurements, are consistent with ADCP wave measurements (Fig. 2b). The timing and the duration of the wave signal, measured from both bottom-pressure and ADCP surface wave measurements, agreed remarkably well.

c. *Mixed layer depth and background currents*

The stratification was strong and mixed layer depth (hereafter referred as MLD or subscript D) was shallow (~10–15 m) during the summer months (Fig. 4a). The stratification became weak and the mixed layer deepened during the passage of atmospheric fronts in fall of

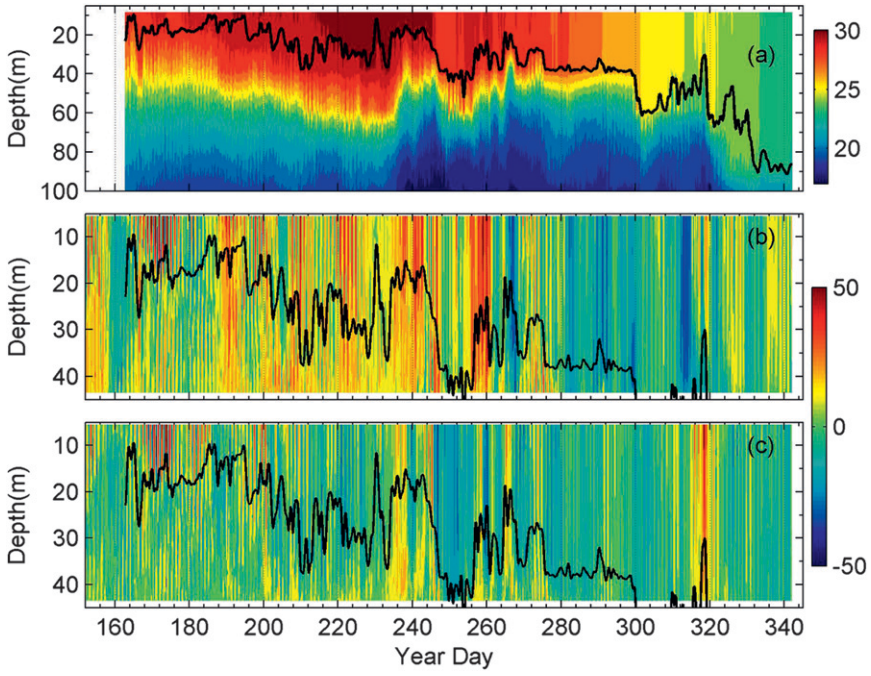

FIG. 4. (a) The color shading shows the time–depth temperature (°C) at S2 and thick black line denotes mixed layer depth. Low-pass-filtered (b) east–west U and (c) north–south V velocity components (cm s^{-1}) at M5 where water depth is 47 m. Cutoff frequency of low-frequency currents is 0.08 cph. Black lines indicate MLD at S2.

2011. The MLD was estimated from moored temperature time series at S2–S4, because salinity had a negligible impact here on the vertical structure of density (TG). The MLD was computed as the depth at which temperature has decreased by 0.2°C from the shallowest temperature measurement. Estimates of MLD at M2–M4 are similar, and therefore the MLD at M2 is used for this analysis (Fig. 4a). Note that there was not a TCP string mooring at M5, and therefore MLD is inferred from the temperature records at M2–M4 (Fig. 4a). After 28 October (year day 300), the mixed layer around the bank deepened below 47 m, indicating that the water column over the bank was well mixed. A detailed discussion of MLD and its relationships with longer time scale processes are described by TG. In the present study, we use MLD as a scaling parameter that controls the vertical distribution of high-frequency velocity fluctuations in the mixed layer.

TG described low-frequency flows around the bank for 2011. They note that background low-frequency motions were dominated by semidiurnal tides (12.42 h), near-inertial waves (25.58 h), and 60- and 96-h oscillations. In general, barotropic diurnal and semidiurnal tides were weak, and mean surface currents were eastward in the upper 80 m. Mean currents below approximately 20-m above the bottom followed the bathymetry. Figures 4b and 4c show low-frequency horizontal currents at M5. Near-inertial currents were typically stronger and highly baroclinic during summertime when stratification was strong. Once the stratification was broken down during fall and winter seasons, the currents became nearly barotropic with relatively weak shear in the water column.

4. High-frequency velocity fluctuations

Vertical velocity w in the mixed layer over the bank was as large as 10 cm s^{-1} during wind events (Fig. 2e); w is based on 15-min-averaged ADCP measurements. Vertical velocity became strongest when wind speed and Stokes drift velocity were largest (Figs. 2a–d). The squared vertical velocity averaged over water depth w_H^2 clearly correlated with the occurrence of surface waves over the bank. Figures 2d and 2e further illustrate the near-perfect coincidence between the vertical velocity at 5.5 m and the surface wave signature, measured by the bottom-mounted Ppod. A total of 12 wind events with significantly large w_H^2 were identified between June and December 2011 (Fig. 2f). In general, the production-scale turbulent flows in the mixed layer have time scales varying from several minutes to hours. These time scales are determined by the depth of the mixed layer and the dominant turbulent eddies in the mixed layer. Therefore,

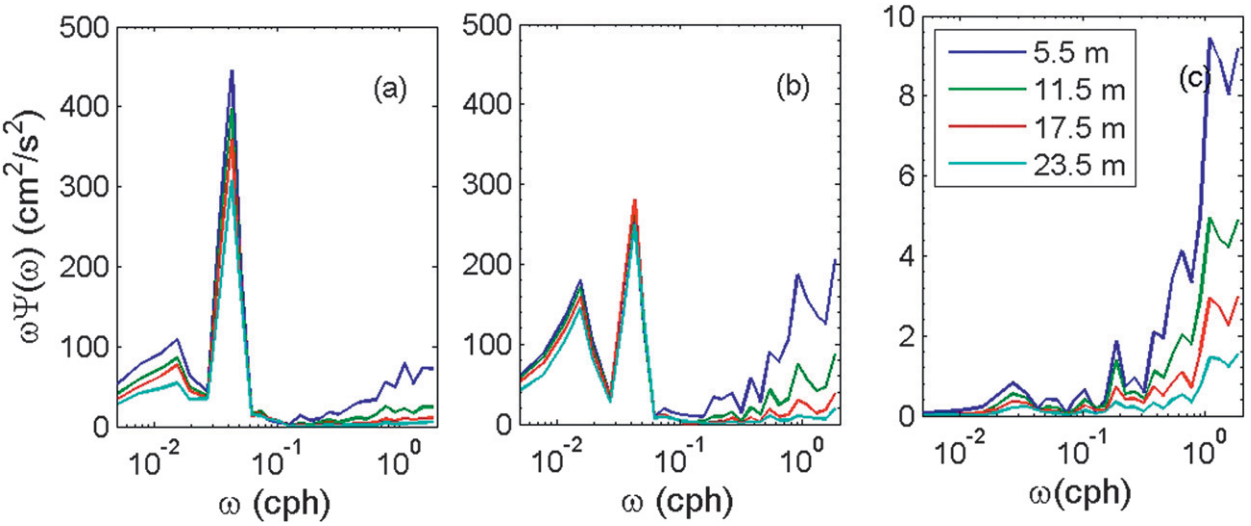

FIG. 5. Variance-preserving frequency spectra: (a) u, (b) v, and (c) vertical w velocity components computed at 5.5-, 11.5-, 17.5-, and 23.5-m water depths for the wind event 4. The inertial frequency is 0.041 cph.

the 15-min sampling rate may partially resolve production-scale turbulent flows in the mixed layer. We suspect that large vertical velocities over the bank were related to wave-induced currents, such as Langmuir flows. According to the theory of Craik and Leibovich (1976), the combined effects of Stokes drift and background vorticity $\mathbf{\Omega}$ of mean currents generates a vortex force $\mathbf{F}$, which drives the Langmuir circulation, where

$$\mathbf{F} = \mathbf{U}_S(z) \times \mathbf{\Omega}. \tag{3}$$

In the following, we examine these high-frequency motions in the mixed layer and their relationships to winds and surface waves.

a. Three-dimensional velocity structure

To examine strength and distribution of velocity variance at higher frequencies, velocity spectra were computed during several wind events. One example, shown in Fig. 5, is the variance-preserving velocity spectra for event 4. A spectrum for a given depth was computed from 512 data points (or 5.33-day record) centered on the wind event. The spectra were multiplied by the corresponding frequencies to construct the variance-preserving spectra, which were then averaged into 32 frequency bands (Fig. 5). Depth–time series of horizontal and vertical velocities for event 4 are plotted in Fig. 6. Low-frequency currents and high-frequency velocity variances are illustrated separately. Low-frequency currents were constructed by removing velocities at higher than 0.08 cph, while high-frequency velocity currents were constructed by removing velocities at frequencies lower than 0.2 cph. A fourth-order Butterworth filter was used for filtering the velocity fields. Velocity spectra show distinct features: (i) spectral peak in horizontal velocity spectra at near-inertial frequency (0.041 cph), and (ii) elevated velocity variance at higher frequencies between 0.2 cph and the Nyquist frequency of 2 cph (Fig. 5). The high-frequency energy levels were largest near the Nyquist frequency, indicating that the 15-min sampling rate would resolve higher-frequency motions partially.

During event 4, winds increased from 4 to 15 m s^{-1}; the southerly winds rotated counter clockwise to form westerly winds in the middle part of event (days 246–247) before veering toward the south during the latter part of the event (Fig. 2). The mixed layer deepened from 20 to 40 m; and low-frequency currents (such as near-inertial waves) as large as 0.5 m s^{-1} were formed. Here, $\langle u^2 \rangle$ was smaller than $\langle v^2 \rangle$, but the strongest values of $\langle u^2 \rangle$ and $\langle v^2 \rangle$ were in the crosswind direction (Figs. 2 and 6); $\langle w^2 \rangle$ varied with winds, but followed Stokes drift closely (not shown). The high-frequency velocity variances ($\langle u^2 \rangle$, $\langle v^2 \rangle$, and $\langle w^2 \rangle$) decreased rapidly with depth; for example, a couple of orders of magnitude difference in variance of $\langle w^2 \rangle$ were found between 5.5- and 40-m water depths (Fig. 6). Here, $\langle w^2 \rangle$ penetrated to greater depths than $\langle u^2 \rangle$ and $\langle v^2 \rangle$. At the sea surface w must be zero and has a subsurface maximum between the surface and 5.5 m, because w decays with depth starting at 5.5-m depth. Furthermore, high-frequency motions were strong when near-inertial waves were large (Fig. 6). We suspect that the advection of high-frequency velocity variances by near-inertial currents might be an important term in the energy balance of high-frequency motions.

We further examined other wind events to understand the three-dimensional velocity structure in the mixed

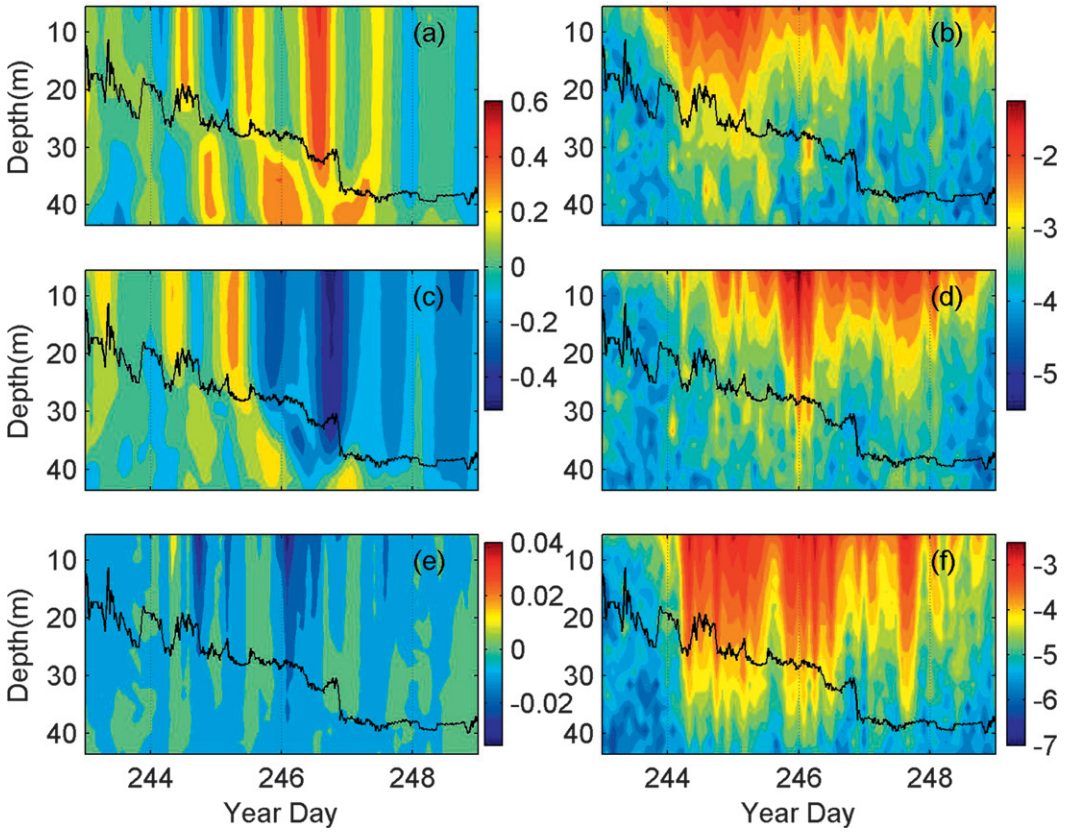

FIG. 6. Depth–time sections of currents at M5 during wind event 4. (left) Low-pass filtered currents (a) U, (c) V, and (e) W ($\mathrm{m\,s^{-1}}$). East, north, and upward directions are positive. (right) Log_{10} values of squared high-frequency (denoted by angle brackets) currents ($\mathrm{m\,s^{-1}}$) (b) $\log_{10}(\langle u^2\rangle)$, (d) $\log_{10}(\langle v^2\rangle)$, and (f) $\log_{10}(\langle w^2\rangle)$. The black lines denote the MLD. The cutoff frequency of high-frequency fluctuations is set to 0.2 cph.

layer. Figure 7 illustrates two examples of depth–time variability of $\langle u^2\rangle$, $\langle v^2\rangle$, and $\langle w^2\rangle$, and magnitudes and directions of Stokes drift and surface currents. During the summer event (event 2) the winds/Stokes drifts were approximately from the south and the mixed layer was shallow (~20 m) (Figs. 7a–d); between year day 178 and 179, mixed layer low-frequency currents were approximately 90° out of phase with Stokes drift; after year day 179, mixed layer currents were dominated by clockwise-rotating, near-inertial motions, and increasing mean flow (Fig. 7e). Stokes drift of about 3–5 $\mathrm{cm\,s^{-1}}$ was from the southwest, and reduced to below 2 $\mathrm{cm\,s^{-1}}$ after year day 181 (Fig. 7a). At the beginning of event 2, both the north–south (crosswind) velocity variance (i.e., $\langle u^2\rangle$) and the east–west (downwind) velocity variance (i.e., $\langle v^2\rangle$) were generated. The vertical velocities were strong and $\langle w^2\rangle$ strengthened, penetrated below the MLD as the Stokes drift increased to above a threshold value (~2 $\mathrm{cm\,s^{-1}}$), and diminished as Stokes drift decreased below the threshold (Fig. 7e). However, there is no apparent relationship between the magnitude of high-frequency motions and the direction of near-inertial currents (Figs. 7c,e,g,i). During the fall event (event 5), the winds/Stokes drifts were approximately from the east and the mixed layer was deep (~40 m). The direction of the surface current was nearly 180° out of phase with the Stokes drift between year day 278 and 281 and those currents became in phase during the later stages (Fig. 7d). At the beginning of event 5, winds/Stokes drift were small; Stokes drift opposed the surface current; and high-frequency velocity components were small. During the latter part of event 5, higher east–west (downwind) (i.e., $\langle u^2\rangle$) and vertical velocity variances were generated as winds/Stokes drift increased and both Stokes drift and the surface current were in the same direction (coming from the east) (Fig. 7d), but the north–south (crosswind) surface current component (i.e., $\langle v^2\rangle$) remained low (Fig. 7j). For a typical Langmuir flow in the open-ocean surface layer, we expect generation of crosswind surface currents, but here we observed a strong downwind surface current (Fig. 7h), perhaps similar to shear-driven turbulence. These examples show the generation of

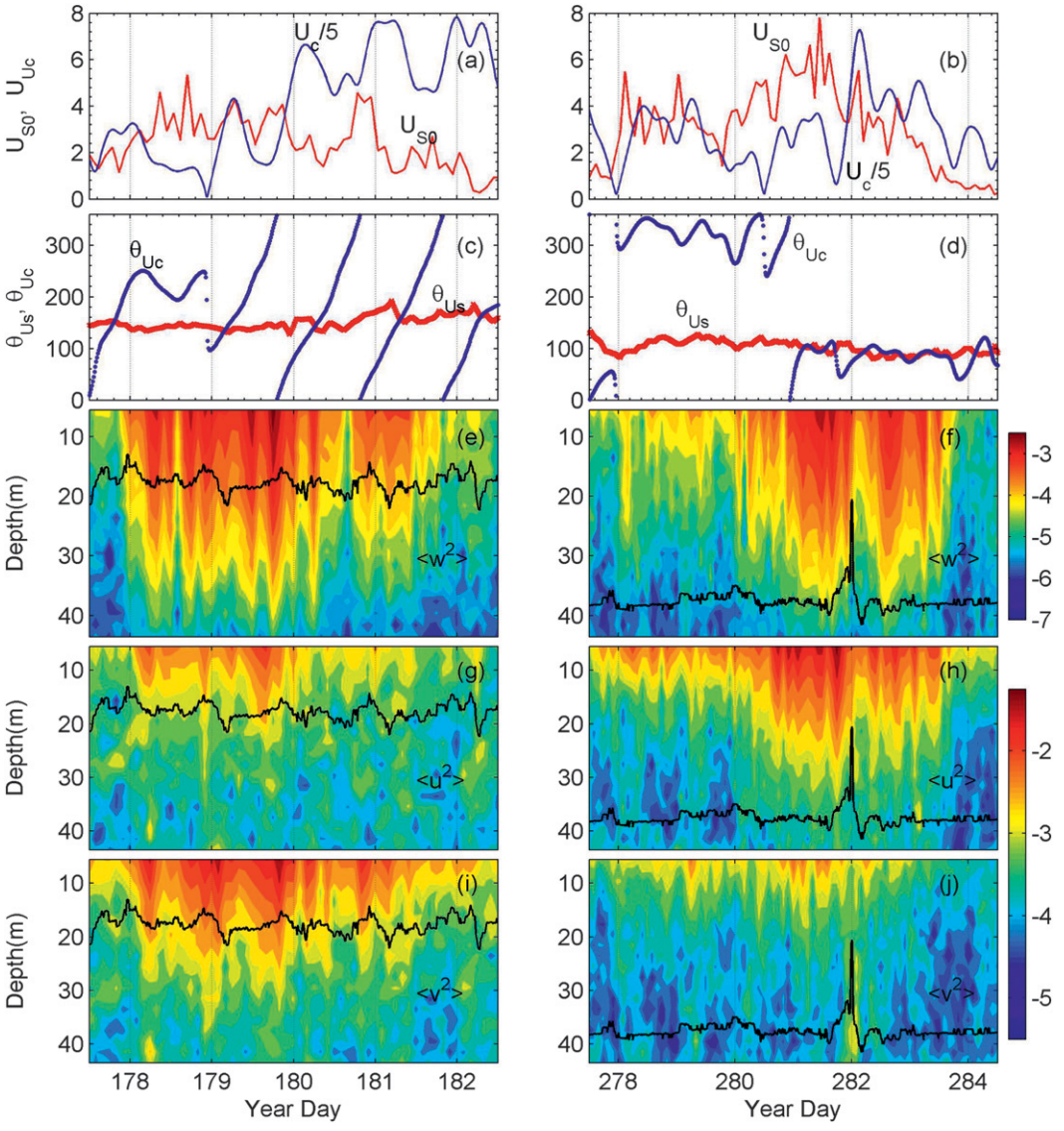

FIG. 7. (a),(b) The magnitude of U_{S_0} (red) and surface current $U_C/5$ (blue) in the upper 15.5 m at M5 (cm s^{-1}) during (left) event 2 and (right) event 5. (c),(d) Corresponding directions (°) of Stokes drift θ_{U_S} (red) and surface current θ_{U_c} (blue). (e)–(j) Corresponding depth–time sections of squared high-frequency currents $\langle w^2\rangle$, $\langle u^2\rangle$, and $\langle v^2\rangle$. Log_{10} values of velocity (m s^{-1}) variances are plotted. Thick black lines denote MLD. Directions follow convention used in meteorology and represent the direction from which the Stokes drift and currents originate.

a three-dimensional complex flow field in the presence of wind events and background currents. However, the timing and the magnitude of velocity variances appear to depend on both strengths and directions of winds and waves over the bank. We further examine high wind events and their parameter dependence on $\langle w^2\rangle$ in section 4e.

b. *Probability distribution*

As discussed above, high-frequency flows observed during wind events were strongest near the surface and decayed rapidly with depth. We also noted that magnitudes of upward and downward motions were comparable. Skewness of w for the 12 events between 5.5 and 15.5 m is -0.34 with a standard deviation 0.36, and the corresponding kurtosis (or flatness) is 4.67 with a standard deviation 0.23. These statistics show that the probability distribution of w differs from the Gaussian distribution (in which skewness is 0 and kurtosis is 3). Figure 8 shows cumulative probability distributions of normalized u, v, and w and the corresponding cumulative normal Gaussian distributions at 5.5-m depth for

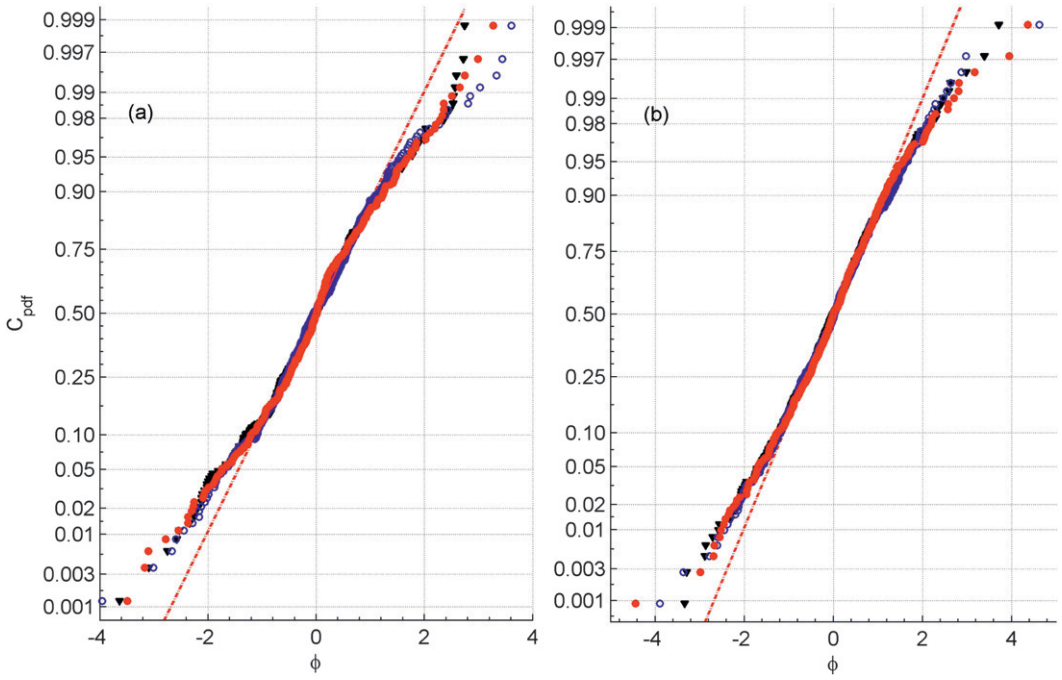

FIG. 8. Cumulative probability distribution function C_{pdf} of high-frequency velocity at 5.5-m depth is plotted against the normalized velocity ϕ for (a) summer event 2, (b) fall–winter event 12. The black triangles, blue open circles, and red dots denote u, v, and w velocity components, respectively. The red dashed line represents the Gaussian distribution function.

two wind events (2 and 12), where the normalized variable $\phi = (\Phi - \overline{\Phi})/\sigma_\Phi$, Φ represents u, v, and w, σ_Φ is the standard deviation, and the overbar denotes the mean of the data record. The events shown in Fig. 8 characterize two different background stratifications and wind/wave patterns (Figs. 2 and 4). Cumulative distributions of u, v, and w are similar, and they all deviate from the Gaussian distribution when $\phi > \sigma_\Phi$, which is nearly 20% of the data record. We noted similar velocity distributions at different depths within the mixed layer. In a turbulent flow, the values of flatness are large relative to a Gaussian distribution if the probability distribution function has relatively large values in its tails (e.g., Fig. 8). The flatness occurs when the time series of the velocity field contains significant numbers of sharp peaks. We suspect that these high-frequency peaks represent production-scale wind-driven turbulent eddies and coherent structures such as Langmuir circulation cells.

c. *Spatial variability*

Figure 9 illustrates high-frequency kinetic energy at M1–M5 for three wind events (2, 4, and 12). Vertical profiles of horizontal kinetic energy (HKE) and vertical kinetic energy (VKE) were computed from high-pass-filtered ADCP velocity profiles. Kinetic energy profiles for these selected events were constructed by time averaging of squared high-pass-filtered velocities (u, v, w), where VKE = $0.5\langle\langle w^2\rangle\rangle$ and HKE = $0.5(\langle\langle u^2\rangle\rangle + \langle\langle v^2\rangle\rangle)$ and $\langle\langle\rangle\rangle$ denotes a time average over wind events. Here, the cutoff frequency was set to 0.2 cph. As we mentioned earlier, these events (Fig. 9) represent different background stratification and wind/wave patterns (Figs. 2 and 4). In event 2, the MLD was shallow (~20 m) and winds were from the south-southeast at an average speed of about 8 m s^{-1}. During event 4, the MLD deepened from 20 to 40 m and winds accelerated from 4 to 15 m s^{-1} while wind and waves rotated clockwise from north to south. During event 12, there was a frontal passage and the water column was well mixed. The high-frequency kinetic energy at M5 was the largest of all mooring observations. The differences in energy were more pronounced in the vertical kinetic energy profiles than in the horizontal kinetic energy profiles. A significantly high energy level at M5 could be caused by the intensification of surface waves over the bank. M5 is located at 47-m water depth and 3-km north of the peak, which is about 20-m below the sea surface. The region north of the peak is a plausible wave-focusing region for waves propagating from the south. We will discuss these wave-focusing effects and their impacts on Stokes drift and vertical velocity in section 5.

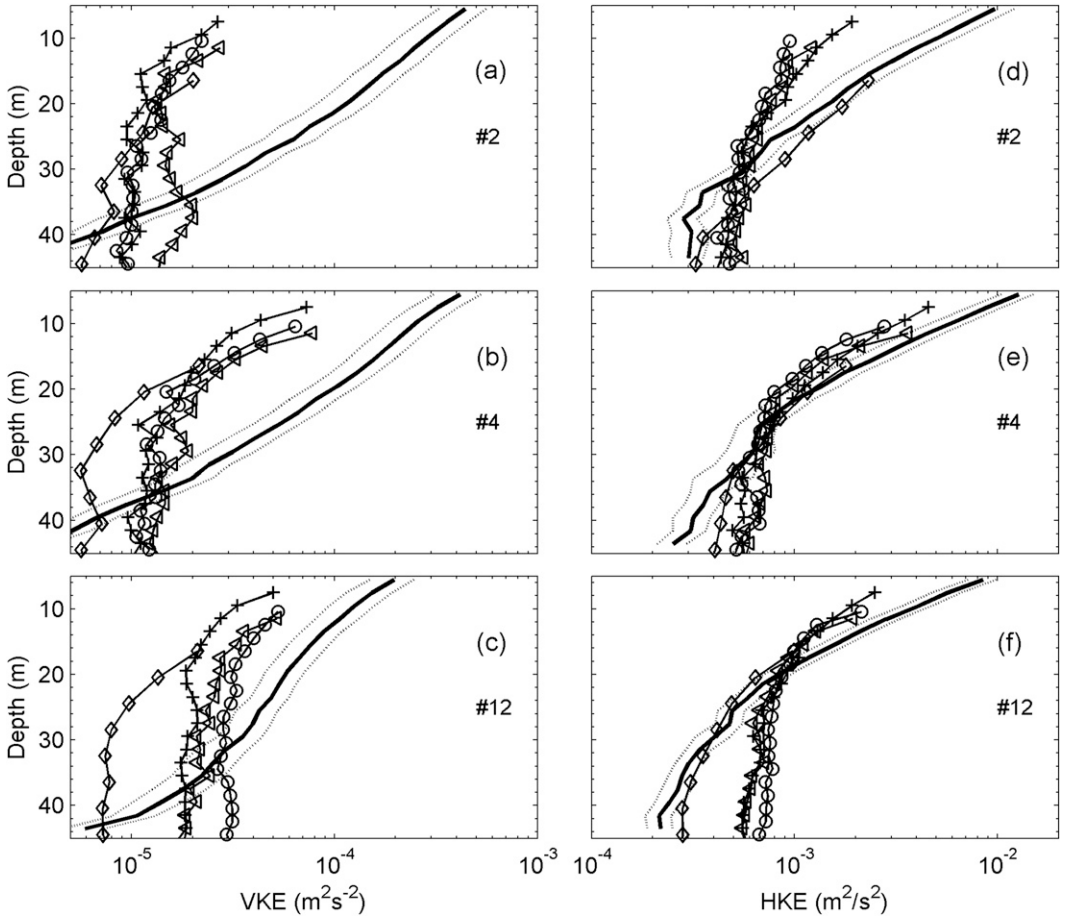

FIG. 9. (a)–(c) Vertical profiles of VKE and (d)–(f) HKE averaged over three wind events [(top) 2, (middle) 4, and (bottom) 12]. Thick solid lines represent energy levels at M5 and dashed lines show 95% confidence limits. Energy levels at M1, M2, M3, and M4 are marked in crosses, open circles, open diamonds, and open triangles, respectively. Confidence limits of energy levels at M1–M4 are not plotted.

d. The e-folding scales

The entrainment depth of vertical velocity can be examined from the *e*-folding length of w^2, because the *e*-folding length compares individual profiles independently of their magnitudes. The *e*-folding length ζ of w^2 was estimated by fitting the exponential profile between the shallowest depth (5.5 m) and 30.5 m, provided that w at the shallowest depth was greater than 3 cm s^{-1}. This minimizes uncertainties of ζ by maintaining well-resolved vertical profiles for the computation. For the Craik and Leibovich (1976) theory, the Langmuir circulation is governed by the vortex force [Eq. (3)], where the magnitude and vertical structure of w^2 depend strongly on Stokes drift [i.e., $\mathbf{U}_S(z)$]. Stokes drift decays exponentially with depth and is a function of horizontal wavelength determined by wave period and water depth. The *e*-folding length η of $|\mathbf{U}_S(z)|$ was also determined by fitting an exponential profile between the surface and 15-m water depth, provided the magnitude of the Stokes drift at the surface (i.e., U_{S_0}) is greater than 1 cm s^{-1}. The *e*-folding length of $|\mathbf{U}_S(z)|$ was also estimated by finding a depth at which $|\mathbf{U}_S(z)|/U_{S_0} = e^{-1}$ (e.g., Harcourt and D'Asaro 2008). Both methods produced comparable estimates of *e*-folding lengths. Note that w^2 profiles were available every 15 min while Stokes drift profiles were available every two hours.

Figure 10 illustrates time series of *e*-folding lengths ζ and η along with the mixed layer depth at S2. The *e*-folding length of w^2 varied between 3.5 and 45 m (Fig. 10b) with an average and a standard deviation of 8.3 and 3.9 m, respectively for the 12 events. Large values of ζ were found with deep MLD (Figs. 10a,b). Because the vertical scale of turbulent eddies depends strongly on the depth of the mixed layer, we can expect large values of ζ for deep mixed layers. The *e*-folding length of $\mathbf{U}_S(z)$ varied between 2 and 9 m (Fig. 10c) with mean $\overline{\eta}$ of 4.45 and standard deviation of 1.02 m, which is

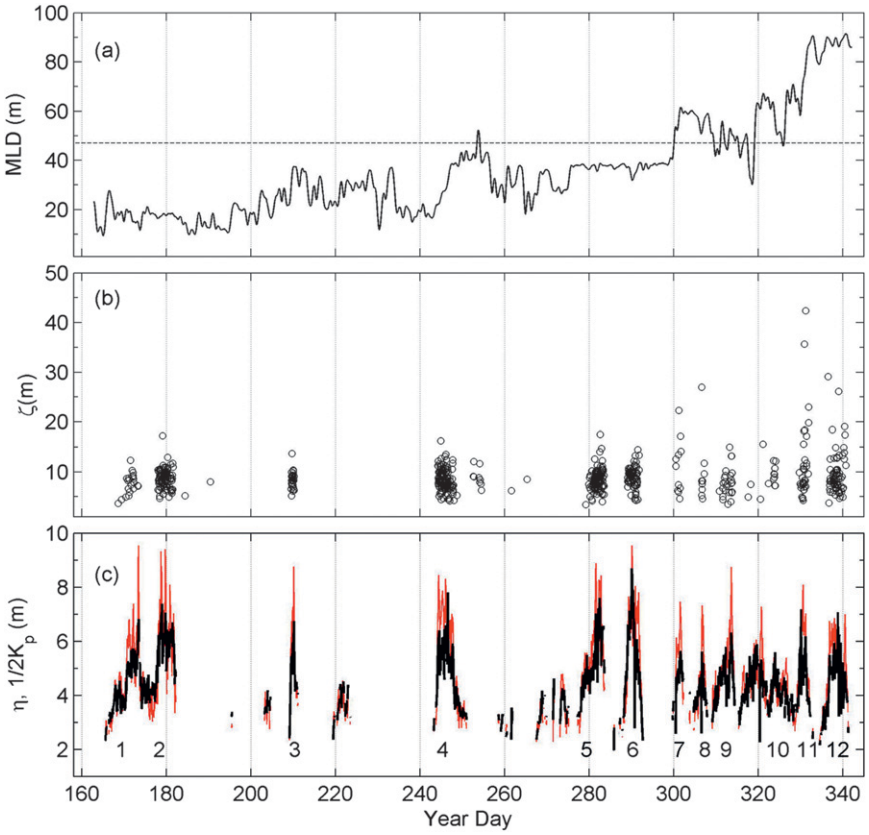

FIG. 10. (a) Time series of MLD at S2. Black dashed line denotes water depth (47 m) at M5. (b) The *e*-folding length (i.e., ζ) of w^2 at M5 for individual profiles. (c) The *e*-folding length of Stokes drift (i.e., η) (black lines) and the vertical scale of the peak wave [$1/(2k_p)$; red lines] at M5. Numbers 1–12 are the wind events marked in Fig. 2.

much less than the mixed layer depth (Fig. 10a). Therefore, wave forcing by the vortex force [Eq. (3)] is limited to the upper 10 m or less. As shown in Fig. 10c, where k_p is the peak wavenumber, the vertical scale of dominant surface wave $(2k_p)^{-1}$ is comparable with η indicating that the vertical structure of the Stokes drift is controlled by the dominant wave. The mean and standard deviation of $(2k_p)^{-1}$ for the 12 events are 4.75 and 1.37 m, respectively. The normalized $\overline{\eta}$ by the mean of $(2k_p)^{-1}$ is about 0.94, which is approximately a factor of 5 larger than the corresponding ratio for the PM spectral model (Li and Garrett 1993). Unlike ζ, η did not change with mixed layer depth but varied with wind speed (Figs. 2 and 10). On average, the vertical kinetic energy penetrated approximately twice the average penetration depth of the Stokes drift. Our observations indicate that the penetration depth of w is determined by several factors, including U_{S_0}, U_*, MLD, and mean currents, while the penetration of the vortex force is determined by the *e*-folding length of the Stokes drift.

e. Scaling vertical velocity

The relative importance of wind and wave forcing is described by the turbulent Langmuir number (McWilliams et al. 1997; Li et al. 2005; Harcourt and D'Asaro 2008),

$$\mathrm{La}_t = (U_*/U_{S_0})^{1/2}. \tag{4}$$

Figure 11 shows La_t versus $\langle w_D^2\rangle/U_*^2$, where $\langle w_D^2\rangle$ was constructed by averaging w^2 over the MLD and then averaging temporally over a 2-h segment before dividing by U_*^2. La_t is based on two-hourly estimates of U_{S_0} and U_*. Almost all of the wind events had $\mathrm{La}_t < 1$, although $\langle w_D^2\rangle/U_*^2$ varied between 0.1 and 60. Our estimate of averaged La_t for the 12 wind events is about 0.63 with a standard deviation of 0.17 (Fig. 11) and is comparable to the estimates of Kukulka et al. (2011) based on measured directional wave spectra with $f_c = 0.4$ Hz. For a fully developed wave field represented by the PM spectral model, La_t is about 0.3 (Li and Garrett 1993; Li et al. 2005). The turbulent Langmuir number is expected

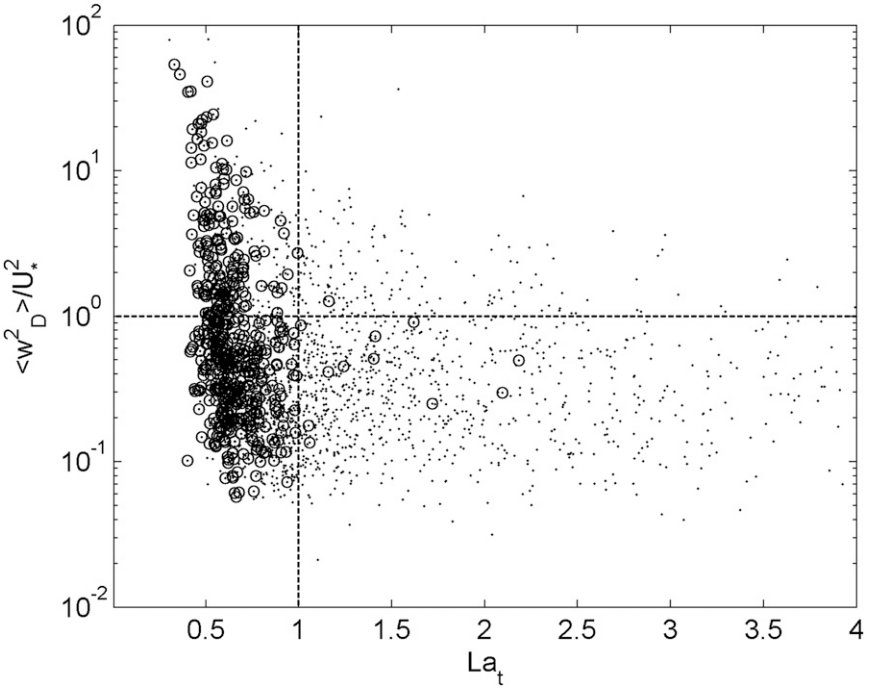

FIG. 11. $\langle w_D^2 \rangle / U_*^2$ vs turbulent La_t. Black dots represent the entire dataset and circles represent data from 12 wind events shown in Fig. 2.

to be higher than 0.3 for developing seas under fetch-limited conditions as a result of weaker Stokes drift (Li et al. 2005; Harcourt and D'Asaro 2008).

Another important scaling parameter is the Hoenikker number (Li et al. 2005), which describes the relative importance of convection (unstable buoyancy forcing) and vortex force driving Langmuir circulation. However, we do not have the net surface buoyancy flux to evaluate the Hoenikker number. We examined day and night variability of $\langle w^2 \rangle$ for cases where $La_t < 1$ and $\langle w_D^2 \rangle / U_*^2 > 1$, but did not find significant differences during wind events.

The vertical velocity is examined within the framework of the wind/wave mechanism such as Langmuir circulation (Craik and Leibovich 1976). This framework is often used to describe the surface velocity variance observed from Doppler sonar systems (e.g., Plueddemann et al. 1996; Smith 1998) and the large-eddy simulation of the oceanic mixed layer, where the vortex forcing is added to mimic Langmuir circulation (Skyllingstad and Denbo 1995; McWilliams et al. 1997; Harcourt and D'Asaro 2008; Grant and Belcher 2009). D'Asaro and Dairiki (1997) and Tseng and D'Asaro (2004) compared MLD averaged and squared vertical velocity with squared friction velocity, and found that on average, $\langle w_D^2 \rangle$ was about a factor of 1.5–3.0 larger than U_*^2, showing the departure from the wall boundary layer theory. Their empirical evidence is somewhat surprising because of lack of dependence on surface wave parameters. Plueddemann et al. (1996) suggest that surface velocity variance scales as $U_* U_{S_0}$, while Smith (1998) reports that velocity variance follows $U_{S_0}^2$ scaling once Langmuir circulation is established. Harcourt and D'Asaro (2008) suggest that turbulent vertical velocity scales as $U_* \mathrm{La}_L^{-2/3}$, where $\mathrm{La}_L = (U_*/\langle U_{SL} \rangle)^{1/2}$, and U_{SL} is the averaged Stokes drift within the surface layer L, which is taken as 20% of the height of the mixed layer. Based on LES studies, Grant and Belcher (2009) report that the velocity scale of Langmuir turbulence can be expressed as $(U_* U_{S_0})^{1/3}$, similar to the scaling suggested by Smith (1996). The observations and modeling studies indicate that there is no consistent scaling for Langmuir cell velocities, even though all these scaling arguments are either related to U_{S_0} or a combination of U_*, U_{S_0}, and mixed layer depth. Here, $\langle w^2 \rangle$ can vary with surface forcing such as Stokes drift, friction velocity, and surface buoyancy flux, and with upper-ocean dynamics such as mixed layer depth and advection caused by mean currents.

We will apply some of the existing scaling methods to the observed vertical velocity in the mixed layer over the bank. We limit our analysis to 12 wind events shown in Fig. 2f where a significant number of good vertical velocity profiles can be found. These wind events occupied a total of about 41 days between June and December 2011. We used 3928, 15-min-averaged w profiles for the analysis. We note that the magnitude and vertical

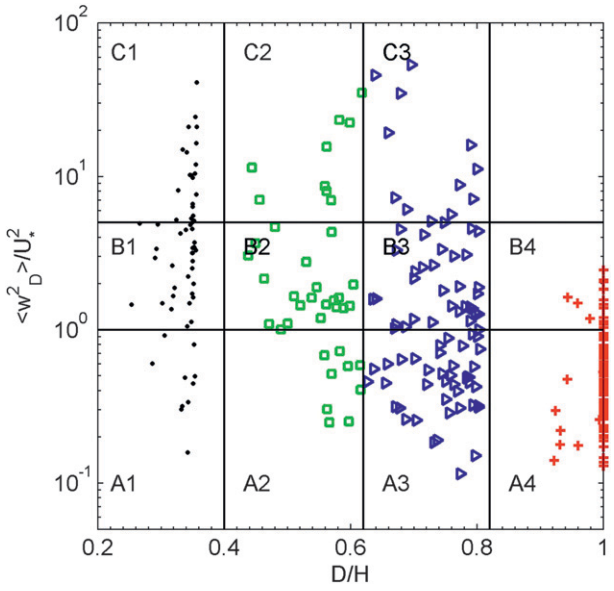

FIG. 12. $\langle w_D^2\rangle/U_*^2$ vs fractional MLD D/H, where A, B, and C represent three groups of $\langle w_D^2\rangle/U_*^2$, and each group is divided into four subgroups of D/H as indicated by 1–4. The colors represent different D/H groups.

structure of w^2 and the magnitudes and directions of Stokes drifts and winds varied significantly within a wind event. Therefore, the scaling of vertical profiles should be conducted by identifying profiles that have similar dynamical regimes or belong to similar parameter regimes defined by the underlying physical process. Figure 12 shows spreading of $\langle w_D^2\rangle/U_*^2$ as a function of D/H, where D/H is the fractional mixed layer depth. The segments cover a broad range of values where $\langle w_D^2\rangle/U_*^2$ ranges from 0.1 to 60 and D/H ranges from 0.2 to 1 (Fig. 12). The vertical velocity profiles were divided into three groups of $\langle w_D^2\rangle/U_*^2$ denoted by A, B, and C (Fig. 12). These groups were selected by considering the mixed layer vertical kinetic energy relative to the wall boundary layer estimates; for example, $\langle w_D^2\rangle/U_*^2 > 1$ represents regimes which depart from wall boundary scaling. As shown in Fig. 12, the data belong to a wide range of mixed layer depths. Therefore, each group was divided into four subgroups representing four different segments of D/H (e.g., A1, A2, A3, and A4 in Fig. 12). For example, the subgroup A1 represents weak energy and shallow mixed layer profiles whereas the group A4 represents weak energy and deep mixed layer profiles. Profiles of $\langle w^2\rangle$ in each subgroup were scaled by U_*^2, $U_*U_{S_0}$, $(U_*^2U_{S_0})^2$, and $U_{S_0}^2$ before constructing averaged profiles.

Scaled $\langle w^2\rangle$ profiles of all subgroups are compared as a function of scaled depth, z/D (Fig. 13). We compare near-surface estimates and the vertical structure of scaled $\langle w^2\rangle$ resulting from U_*^2, $U_*U_{S_0}$, and $U_{S_0}^2$, because the scaling by $U_*U_{S_0}$ and $(U_*^2U_{S_0})^2$ produce relatively similar results. The averaged profiles of $\langle w^2\rangle$, scaled by U_*^2, $U_*U_{S_0}$, and $U_{S_0}^2$, are plotted in Figs. 13a–c, Figs. 13d–f, and Figs. 13g–i, respectively. These contain profiles from groups A, B, and C (see Fig. 12), respectively. There is a fair qualitative agreement with U_*^2 scaling for group A (Fig. 13a). Here, $\langle w^2\rangle/U_*^2$ profiles in group A collapse to a single curve in the upper half of MLD. However, U_*^2 scaling fails for $\langle w^2\rangle/U_*^2 > 1$ (Figs. 13b,c). The scaling of $\langle w^2\rangle$ by $U_*U_{S_0}$ is also qualitatively consistent with group A even though near-surface estimates are slightly smaller than the expected estimate of unity (Fig. 13d). Scaling of $U_*U_{S_0}$ over predicts slightly for B1, B3, and B4 (Fig. 13e). Like U_*^2 scaling, $U_*U_{S_0}$ does not provide a satisfactory agreement for group C, where $\langle w^2\rangle/U_*U_{S_0}$ near the surface is about 10. There is a wide range of values for $\langle w^2\rangle/U_{S_0}^*$ for groups A and B, but $\langle w^2\rangle/U_{S_0}^2$ near the surface is close to unity for subgroups A2, A4, B1, B2, and B4. None of the scaling methods works well for group C, nevertheless $U_{S_0}^2$ scaling provides near-surface estimates of $\langle w^2\rangle/U_{S_0}^2$ close to a factor of 2. In most of the groups, the vertical structure of scaled profiles decays with varying e-folding scales. These results reflect the fact that there is no unique scaling of $\langle w^2\rangle$ profiles in the mixed layer based on surface forcing parameters, although $\langle w^2\rangle$ depends on U_*, U_{S_0}, mixed layer depth, and e-folding scales of w^2.

Wind events generate near-inertial currents (e.g., Fig. 5), and the relative direction between winds and surface currents can make a difference in the vertical shear of horizontal currents which in turn can alter turbulence production in the mixed layer. This scenario could be a plausible explanation why our parameterizations were significantly different from previous publications. We examined the impact of low-frequency (near inertial) currents on high-frequency vertical velocity by examining correlations between vertical velocity and directional difference between winds and near-surface currents. Relations among wind and surface current directions, wind speed, and variability of high-frequency flows for 12 events (Fig. 2) were examined. We did not find a clear relation between the angular difference of the mixed layer current and wind speed, and $\langle w^2\rangle$ during different stages of wind events. The difference between wind and current directions were computed from 2-h-averaged current and wind fields. Here, near-surface currents at M5 were constructed by depth-averaging low-pass-filtered horizontal currents between 5.5 and 15.5 m.

5. Discussion

a. Vertical scaling

Scaling of $\langle w^2\rangle$ by surface-forcing parameters such as friction velocity and Stokes drift produced inconclusive

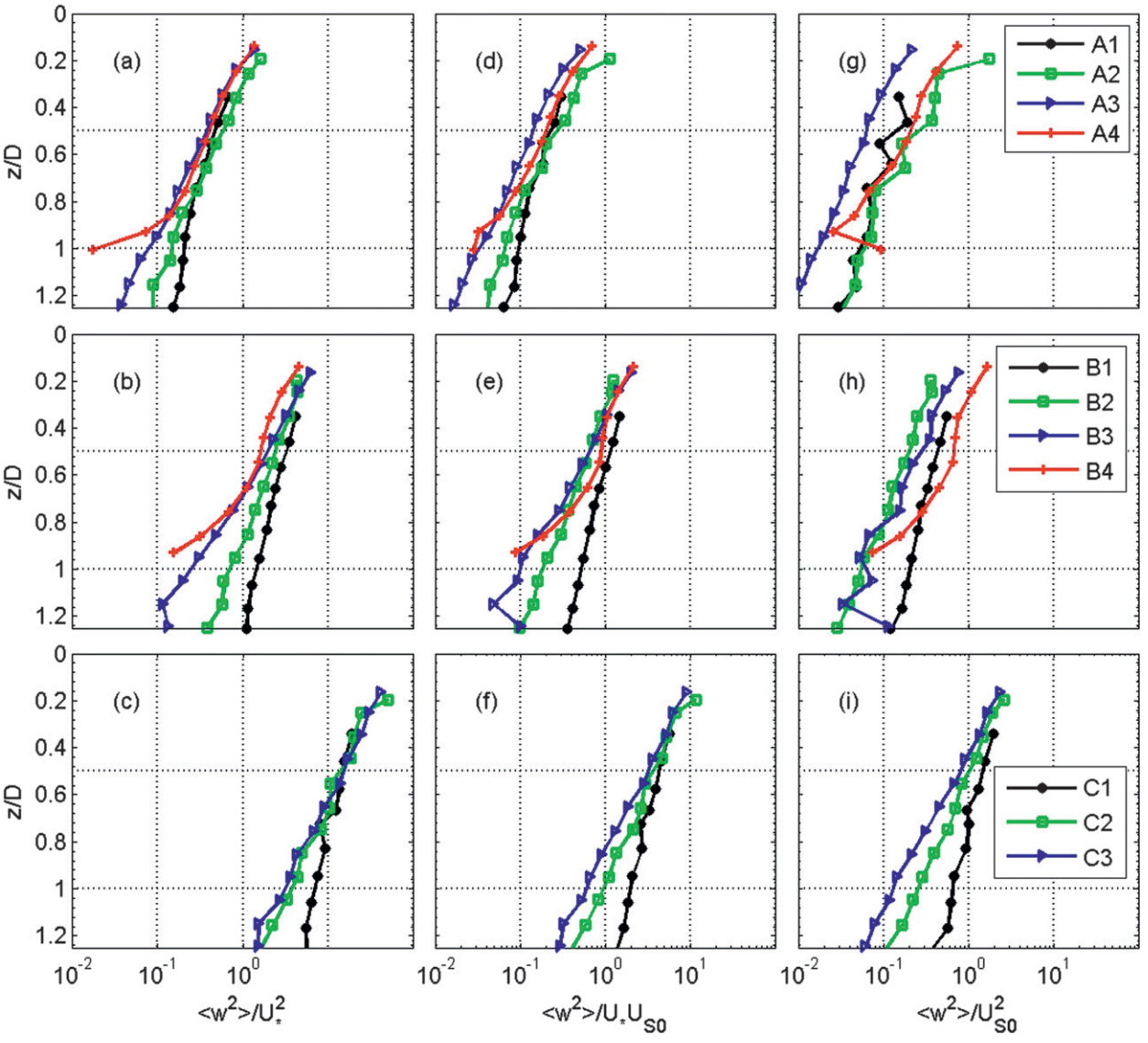

FIG. 13. Scaled squared vertical velocity plotted as a function of scaled water depth (z/D) (a)–(c) U_*^2 scaling for groups A, B, and C, respectively, (d)–(f) $U_*U_{S_0}$ scaling, and (g)–(i) $U_{S_0}^2$ scaling are represented. Colored symbols represent regions of D/H as marked in Fig. 12.

results. We note that the *e*-folding scale of $\langle w^2 \rangle$ has a wider range and varies with the mixed layer depth. For example, profiles in groups B and C have higher energy levels at depth than the rest of the profiles. The vertical distribution of $\langle w^2 \rangle$ should also be considered when scaling $\langle w^2 \rangle$ (e.g., D'Asaro and Dairiki 1997; Harcourt and D'Asaro 2008), because individual profiles of w^2 have diverse *e*-folding scales and are associated with different mixed layer depths (Fig. 9). Therefore, we consider mixed layer–averaged statistics such as squared vertical velocity $\langle w_D^2 \rangle$ as our variable to be scaled and then examine the variability of scaled $\langle w_D^2 \rangle$ as a function of the *e*-folding length scale of w^2 and the mixed layer depth. Figure 14 illustrates $\langle w_D^2 \rangle / U_*^2$ versus ζ/D and $\langle w_D^2 \rangle / U_{S_0}^2$ versus ζ/D where ζ/D is the fractional *e*-folding length. For $\langle w_D^2 \rangle / U_*^2 < 1$, the scaling by U_*^2 provides a tighter relationship with ζ/D (Fig. 14a), which is consistent with Fig. 13a, but U_*^2 scaling fails for $\langle w_D^2 \rangle / U_*^2 > 1$. The scaling by $U_{S_0}^2$ forces close fitting between $\langle w_D^2 \rangle / U_{S_0}^2$ and ζ/D. As shown in Fig. 14b, $\log(\langle w_D^2 \rangle / U_{S_0}^2)$ is approximately a linear function of ζ/D, and the least squares fit to the data is

$$\frac{\langle w_D^2 \rangle}{U_{S_0}^2} = \alpha \, \mathrm{Exp}\left(\beta \frac{\zeta}{D}\right), \tag{5}$$

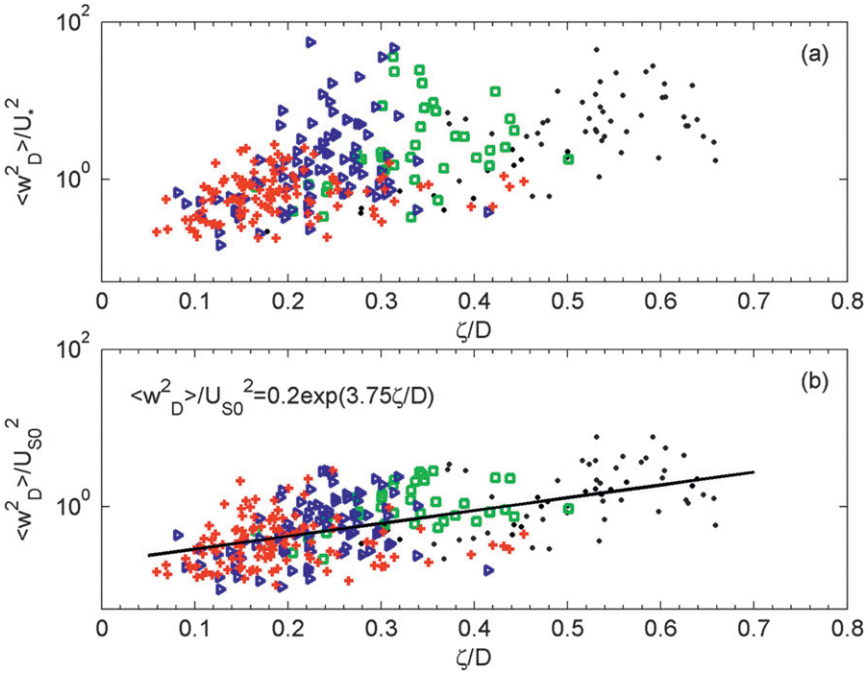

FIG. 14. (a) $\langle w_D^2\rangle/U_*^2$ vs ζ/D (normalized e-folding length of $\langle w^2\rangle$ by mixed layer depth). (b) $\langle w_D^2\rangle/U_{S_0}^2$ vs ζ/D. The colored symbols represent groups of fractional mixed layer depth D/H as marked in Fig. 12. The thick solid line in (b) represents the least squares exponential fit.

where $\alpha = 0.2, \beta = 3.75$, and $0 < \zeta/D \leq 1$. In general, $U_{S_0}^2$ scaling provides a better representation of data, when effects of the mixed layer depth and the penetration depth of the vertical velocity are included.

b. *Wave focusing over the bank*

We noted that high-frequency kinetic energy over the bank at M5 is significantly larger than the kinetic energy around the bank, and these differences can be clearly seen in the vertical kinetic energy, especially when winds were from the south-southeast (Fig. 8). We suspect that these higher velocity fluctuations are generated by wave–current interaction mechanisms defined by the vortex force [Eq. (3)]. The amplitude of the vertical component of the vortex force is $F_v = |\mathbf{U}_S(z)\partial\overline{U}_m/\partial z|$, where $|\mathbf{U}_S(z)|$ is the amplitude of the Stokes drift and $\partial\overline{U}_m/\partial z$ is the vertical gradient of the mean current in the direction of the Stokes drift. To examine the influence of $\partial\overline{U}_m/\partial z$ on F_v, these gradients are compared at different sites. As shown in Fig. 15, all five moorings sites over and around the bank had similar profiles of vertical shear of the mean currents. Components of vertical shear were computed from centered differencing of low-pass-filtered ADCP records, where, the squared shear of the mean current is $\mathrm{Sh}^2 = (\partial\overline{U}_m/\partial z)^2 = [(\partial U/\partial z)^2 + (\partial V/\partial z)^2]$ (Fig. 15). The low-frequency shear is dominated by near-inertial currents and is largest at the base of the mixed layer. Shear profiles vary with wind events and background stratification, but the magnitude and vertical structure of shear profiles are relatively similar for all mooring sites. Therefore, it is unlikely that $\partial\overline{U}_m/\partial z$ alone generates a larger vertical velocity over the bank than at other locations around the bank.

The propagation of surface waves over complex bottom bathymetric features may be associated with many processes including shoaling, refraction, energy dissipation, and diffraction. We suspect that waves coming from the south (from southwest to southeast) generate a focusing region behind the peak of the bank, while enhancing surface wave amplitudes and Stokes drift. To examine the plausibility of wave focusing, we apply a refraction and diffraction numerical wave model (REF/DIF1) developed by Kirby and Dalrymple (1994). REF/DIF1 is a phase-resolving parabolic refraction–diffraction model for ocean surface wave propagation.

We apply REF/DIF1 to a domain of 14 km (north–south) by 10 km (east–west) encompassing the EFGB (Fig. 1) with the x axis as the offshore boundary for incoming waves. The surface Stokes drift for a monochromatic wave can be estimated as $U_{S_0} = a^2k\omega$, where a is the amplitude of the monochromatic wave, k is the wavenumber, and ω is the radian frequency. Note the wave height is twice the wave amplitude.

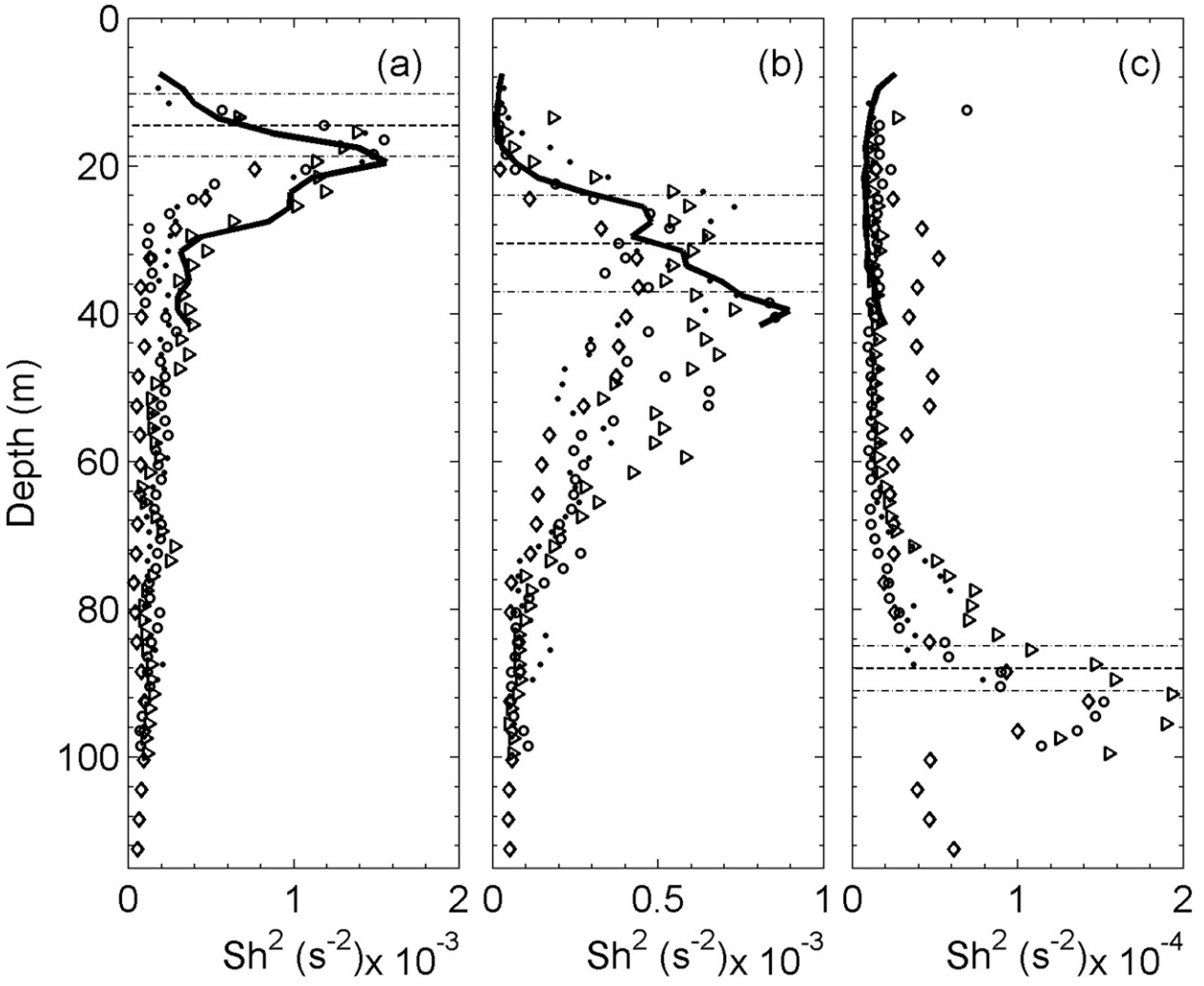

FIG. 15. Squared vertical shear (i.e., Sh^2) of low-frequency horizontal currents at M1–M5 for three different wind events: (a) 2, (b) 4, and (c) 12. Bullets, open circles, diamonds, triangles, and thick solid line denote M1, M2, M3, M4, and M5, respectively. Thick dashed lines denote mean MLD at M2 mooring and thin dashed lines denote one std dev from the mean.

Figure 16 shows simulation results of wave height and Stokes drift for a representative monochromatic wave of 1-m amplitude (or 2-m wave height) and 8-s wave period, propagating from the southern boundary into the model domain. The selected wave statistics are similar to the waves statistics observed during event 2 (Fig. 2). The model results display the spatial variation of wave height and Stokes drift induced by the depth changes from the presence of the bank. The northward-propagating wave focuses over a narrow area behind the peak of the bank while generating a much higher wave height and Stokes drift. The wave height in the focusing area reaches 3 m which is a 50% increase over the incoming wave. The surface Stokes drift increases to 12 cm s^{-1}, which is approximately a factor of 2.5 higher than that of the incoming wave. Several sensitivity REF/DIF1 simulations were also conducted by changing the incoming wave direction by ±15°. Similar narrow band wave-focusing zones were found. Out of five moorings, only one mooring (M5) is in the vicinity of the focusing zone. Our simulation is limited to a monochromatic wave train with a single direction and no background currents. Nevertheless this simulation demonstrates the underlining physical process. It is likely that the observations of high energy levels of kinetic energy at M5 would be a result of enhancement of Stokes drift caused by wave focusing induced by the bathymetric variation of the EFGB.

c. *Impact of vertical motion on corals*

The EFGB marine sanctuary is a biologically diverse environment and supports a large number of species including corals. Coral reefs are complex, dynamic, and

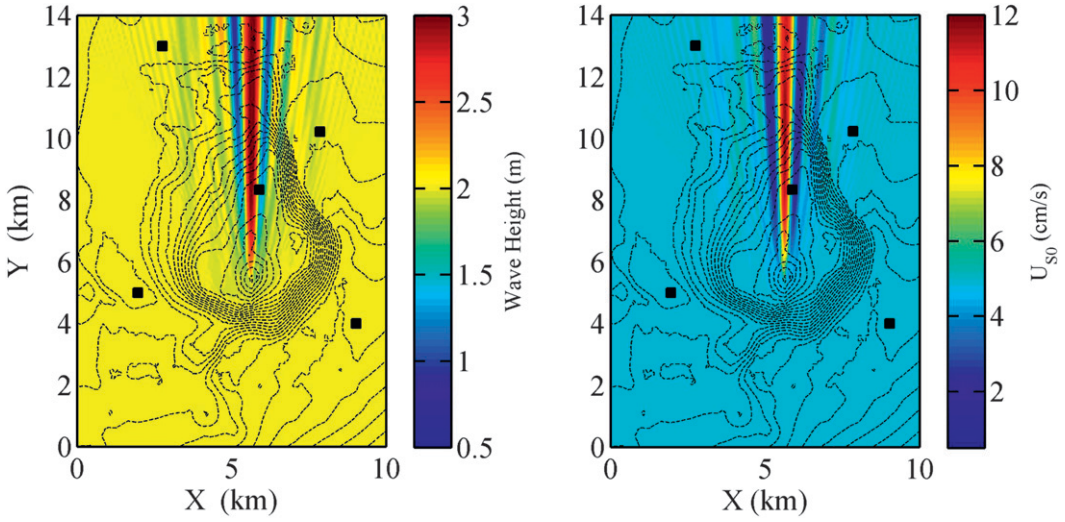

FIG. 16. Color shading shows spatial variations of (left) wave height and (right) Stokes drift from REF/DIF1 simulations. Thin dashed black contours show the bathymetry of EFGB. Black squares are the locations of Barny moorings (M1–M5) and M5 is located over the bank (see also Fig. 1).

sensitive ecosystems. Therefore understanding of the hydrodynamics, turbulence characteristics, mixing of water masses over banks, and transport of suspended sediment are important for the coral reef system. Wave–current interactions and generation of deeply penetrating vertical motions can play an important role in mixing, rapid deepening of the mixed layer, and vertical transports of near-surface water toward coral habitats on the bottom. Vertical velocities intensify during wind events, while wave focusing can further enhance wave-driven Stokes drift thus providing an efficient mixing and transport mechanism over the bank.

6. Conclusions

The main objectives of this study are as follows: (i) to examine surface wave effects on high-frequency flows over the EFGB, (ii) to quantify spatial and temporal characteristic of these high-frequency flows, and (iii) to examine the scaling laws of vertical velocity based on the Langmuir circulation theory. The major observational findings and inferences of this study are the following.

- High-frequency, three-dimensional flows with frequencies ranging from 0.2 to 2 cph (Nyquist frequency) were found in the mixed layer when wind speed and Stokes drift were large. It is suggested that Stokes drift and mean flow interactions such as Langmuir circulation are responsible for generating the observed velocity fluctuations.
- Stokes drift over the bank was estimated from two-dimensional directional wave spectra from a 600-kHz ADCP. The estimated Stokes drift at the surface (i.e., U_{S_0}) varied with the wind speed and is about 0.6% of the wind speed for winds greater than $10\,\mathrm{m\,s^{-1}}$. However, our estimates are a factor of 2 smaller than the estimates based on the PM spectral model.
- Vertical velocity fluctuations showed upward and downward motions with similar magnitudes. The probability distribution of velocity fluctuations (u, v, w) departs from the Gaussian distribution especially at the tail ends of the distribution.
- Squared vertical velocity w^2 was strongest near the surface and decayed exponentially with depth, and the associated e-folding length is a factor of 2 larger than the e-folding length associated with Stokes drift.
- The 2-h and mixed layer–averaged $\langle w_D^2 \rangle$, normalized by the squared friction velocity U_*^2, varied from 0.1 to 60. The $\langle w_D^2 \rangle / U_*^2$ was strongest when the turbulent Langmuir number was less than unity and the mixed layer was shallow.
- Scaling of squared vertical velocity profiles was examined as functions of U_*, U_{S_0}, and $U_{S_0}^2$. Although w^2 is likely to be a function of Stokes drift, U_*, and mixed layer depth, a unique scaling for profiles of w^2 was not found. For $\langle w_D^2 \rangle / U_*^2 < 5$, there is a qualitative agreement with different scaling for wide ranges of the fractional MLD. For $\langle w_D^2 \rangle / U_*^2 > 5$, all the scaling techniques underpredict near-surface estimates of w^2. However, when we consider mixed layer–averaged statistics such as squared vertical velocity $\langle w_D^2 \rangle$ as the scaling variable, the scaling by $U_{S_0}^2$ forces tighter relationships between $\langle w_D^2 \rangle / U_{S_0}^2$ and ζ/D, and $\langle w_D^2 \rangle / U_{S_0}^2$

is approximately an exponential function of ζ/D. In general, $U_{S_0}^2$ scaling provides a better representation of $\langle w_D^2 \rangle$ data, when effects of the mixed layer depth and the penetration depth of the vertical velocity are included.

- Largest velocity variances were found over the bank at M5, located nearly 3 km north of the peak of the bank. It is suggested based on a wave refraction–diffraction model (REF/DIF1) that the increase in kinetic energy over the bank is due to enhancement of Stokes drift by topography-induced waves focusing.
- The lack of agreement with open-ocean parameterizations of vertical kinetic energy over the bank is likely due to the enhancement of kinetic energy resulting from localized focusing of surface waves.

Wave-driven velocity fluctuations play an important role in mixing and vertical transports and, in addition, can strongly impact coral habitats over the EFGB. Our study reveals that such velocity fluctuations over the bank are closely related to surface wave conditions that can have strong localized variability as a result of wave focusing over the bank. Our findings indicate that the scaling of wave-induced mixed layer currents over a shelf edge bank differs from the open ocean. Recently, Belcher et al. (2012) examined the global perspective of Langmuir turbulence in the ocean surface boundary layer using LES and diagnostic analysis techniques. However, the lack of understanding of detailed physical process suggests that further studies are needed for the generalization of wave-driven mixing processes in the coastal environment.

Acknowledgments. This work was sponsored by the Office of Naval Research in a Naval Research Laboratory (NRL) project referred to as ''Mixing Over Rough Topography (MORT)'' and by the Bureau of Ocean Energy Management (BOEM; formerly Minerals Management Service) in the project referred to as ''Currents Over Banks (COB)'' through the Interagency Agreement M10PG0003. Support for James Moum was provided through ONR Grant N00014-09-1-0280. The measurements were made in cooperation with the Flower Garden Banks National Marine Sanctuary, administered by the National Oceanic and Atmospheric Administration (NOAA). Support provided by Alexis Lugo Fernandez of BOEM and Emma Hickerson of NOAA were greatly appreciated. We thank Mark Hulbert, Steve Sova, Andrew Quaid, and Justin Brodersen for their technical support in mooring preparations and successful deployments. We also thank the captain, crew, and marine technician of the R/V *Pelican* and crew of R/V *Manta* for their assistance. We thank the two anonymous reviewers for their thorough and careful review of the manuscript, and useful comments.

REFERENCES

Agrawal, Y. C., E. A. Terray, M. A. Donelan, P. A. Hwang, A. J. Williams III, W. M. Drennan, K. K. Kahma, and S. A. Kitaigorodskii, 1992: Enhanced dissipation of kinetic energy beneath surface waves. *Nature,* **359,** 219–220.

Anis, A., and J. N. Moum, 1995: Surface wave–turbulence interactions: Scaling ε(z) near the sea surface. *J. Phys. Oceanogr.,* **25,** 2025–2045.

Belcher, S. E., and Coauthors, 2012: A global perspective on Langmuir turbulence in the ocean surface boundary layer. *Geophys. Res. Lett.,* **39,** L18605, doi:10.1029/2012GL052932.

Brubaker, J. M., 1987: Similarity structure in the convective boundary layer of a lake. *Nature,* **330,** 742–745.

Craik, A. D. D., and S. Leibovich, 1976: A rational model for Langmuir circulations. *J. Fluid Mech.,* **73,** 401–426.

D'Asaro, E., and G. Dairiki, 1997: Turbulence intensity measurements in a wind-driven mixed layer. *J. Phys. Oceanogr.,* **27,** 2009–2022.

Dillon, T. M., J. G. Richman, C. G. Hansen, and M. D. Pearson, 1981: Near-surface turbulence measurements in a lake. *Nature,* **290,** 390–392.

Drennan, W. M., M. A. Donelan, K. B. Katsaros, and E. A. Terray, 1996: Oceanic turbulence dissipation measurements in SWADE. *J. Phys. Oceanogr.,* **26,** 808–815.

Earle, M. D., K. E. Steele, and D. W. C. Wang, 1999: Use of advanced directional wave spectra analysis methods. *Ocean Eng.,* **26,** 1421–1434.

Gargett, A. N., and J. R. Wells, 2007: Langmuir turbulence in shallow water. Part 1. Observations. *J. Fluid Mech.,* **576,** 27–61, doi:10.1017/S0022112006004575.

Grant, A. L. M., and S. E. Belcher, 2009: Characteristics of Langmuir turbulence in the ocean mixed layer. *J. Phys. Oceanogr.,* **39,** 1871–1887.

Harcourt, R. A., and E. A. D'Asaro, 2008: Large-eddy simulation of Langmuir turbulence in pure wind sea. *J. Phys. Oceanogr.,* **38,** 1542–1562.

Hunter, R. E., and G. W. Hill, 1980: Near-shore current pattern off south Texas: An interpretation from aerial photographs. *Remote Sens. Environ.,* **10,** 115–134.

Hwang, P. A., 2011: A note on the ocean surface roughness spectrum. *J. Atmos. Oceanic Technol.,* **28,** 436–443.

Kenyon, K. E., 1969: Stokes drift for random gravity waves. *J. Geophys. Res.,* **74,** 6991–6994.

Kirby, J. T., and R. A. Dalrymple, 1994: Combined Refraction-Diffraction Model REF/DEF1, version 2.5. University of Delaware. Center for Applied Coastal Research Documentation and User's Manual Rep. 94–22, 172 pp. [Available online at http://chinacat.coastal.udel.edu/programs/nearcom/wave_module_refdif1.html.]

Kukulka, T., A. J. Plueddemann, J. H. Trowbridge, and P. P. Sullivan, 2011: The influence of crosswind tidal currents on Langmuir circulation in a shallow ocean. *J. Geophys. Res.,* **116,** C08005, doi:10.1029/2011JC006971.

Langmuir, I., 1938: Surface motion of water induced by wind. *Science,* **87,** 119–123.

Leibovich, S., 1983: The form and dynamics of Langmuir circulations. *Annu. Rev. Fluid Mech.,* **15,** 391–427.

Li, M., and C. Garrett, 1993: Cell merging and jet/downwelling ratio in Langmuir circulation. *J. Mar. Res.,* **51,** 737–769.

——, ——, and E. Sykllingstad, 2005: A regime diagram for classifying turbulent eddies in the upper ocean. *Deep-Sea Res. I,* **52,** 259–278, doi:10.1016/j.dsr.2004.09.004.

Lombardo, C. P., and M. C. Gregg, 1989: Similarity scaling of viscous and thermal dissipation in a convecting surface boundary layer. *J. Geophys. Res.,* **94** (C5), 6273–6284.

Lumley, J. L., and H. A. Panofsky, 1964: *The Structure of Atmospheric Turbulence.* Wiley-Interscience, 239 pp.

Marmorino, G. O., G. B. Smith, and G. J. Lindemann, 2005: Infrared imagery of large-aspect-ratio Langmuir circulation. *Cont. Shelf Res.,* **25,** 1–6, doi:10.1016/j.csr.2004.08.002.

McWilliams, J. C., P. P. Sullivan, and C.-H. Moeng, 1997: Langmuir turbulence in the ocean. *J. Fluid Mech.,* **334,** 1–30.

Mellor, G. L., and T. Yamada, 1982: Development of a turbulent closure models for planetary boundary layers. *J. Atmos. Sci.,* **31,** 1791–1806.

Melville, W. K., 1996: The role of surface-wave breaking in air-sea interaction. *Annu. Rev. Fluid Mech.,* **28,** 279–321.

Moum, J. N., and J. D. Nash, 2008: Seafloor pressure measurements of nonlinear internal waves. *J. Phys. Oceanogr.,* **38,** 481–491.

Perkins, H., F. De Strobel, and L. Gauldesi, 2000: The barny sentinal trawl-resistant ADCP bottom mount: Design, testing, and application. *IEEE J. Oceanic Eng.,* **25,** 430–436.

Pierson, W. J., and L. Moskowitz, 1964: A proposed spectral form for fully developed wind seas based on the similarity theory of S. A. Kitaigorodskii. *J. Geophys. Res.,* **69,** 5181–5190.

Plueddemann, A. J., J. A. Smith, D. M. Farmer, R. A. Weller, W. R. Crawford, R. Pinkel, S. Vagle, and A. Gnanadesikan, 1996: Structure and variability of Langmuir circulation during the surface waves processes program. *J. Geophys. Res.,* **101,** 3525–3543.

Pollard, R., and K. J. H. Thomas, 1989: Vertical circulation revealed diurnal heating of the upper ocean in late winter. Part I: Observations. *J. Phys. Oceanogr.,* **19,** 269–278.

Rascle, N., A. Fabrice, Q. Pierre, and C.-F. Denis, 2008: A global wave parameter database for geophysical applications. Part 1: Wave-current-turbulence interaction parameters for the open ocean based on traditional parameterizations. *Ocean Modell.,* **25** (3–4), 154–171.

Shay, T. J., and M. C. Gregg, 1986: Convectively driven turbulent mixing in the upper ocean. *J. Phys. Oceanogr.,* **16,** 1777–1798.

Skyllingstad, E. D., and D. W. Denbo, 1995: An ocean large-eddy simulation of Langmuir circulations and convection in the surface mixed layer. *J. Geophys. Res.,* **100,** 8501–8522.

——, W. D. Smyth, J. N. Moum, and H. Wijesekera, 1999: Upper-ocean turbulence during a westerly wind burst: A comparison of large-eddy simulation results and microstructure measurements. *J. Phys. Oceanogr.,* **29,** 5–28.

Smith, J. A., 1992: Observed growth of Langmuir circulation. *J. Geophys. Res.,* **97,** 5651–5664.

——, 1996: Observations of Langmuir circulation, waves, and the mixed layer. *The Air Sea Interface: Radio and Acoustic Sensing, Turbulence, and Wave Dynamics,* M. A. Donelan, W. H. Hui, and W. J. Plant, Eds., University of Toronto Press, 613–622.

——, 1998: Evolution of Langmuir circulation during a storm. *J. Geophys. Res.,* **103** (C6), 12 649–12 668.

——, R. Pinkel, and R. A. Weller, 1987: Velocity structure in the mixed layer during MILDEX. *J. Phys. Oceanogr.,* **17,** 425–439.

Soloviev, A., and R. Lukas, 2003: Observation of wave enhanced turbulence in the near surface layer of the ocean during TOGA COARE. *Deep-Sea Res. I,* **50,** 371–395.

——, N. V. Vershinsky, and V. A. Bezverchnii, 1988: Small-scale turbulence measurements in the thin surface layer of the ocean. *Deep-Sea Res.,* **35,** 1859–1874.

Strong, B., B. Brumley, E. A. Terray, and G. W. Stone, 2000: The performance of ADCP-derived directional wave spectra and comparison with other independent measurements. *Proc. MTS/IEEE Oceans 2000 Conf.,* Providence, RI, MTS/IEEE, 1195–1203.

Teague, W. J., H. W. Wijesekera, E. Jarosz, D. B. Fribance, A. Lugo-Fernández, and Z. R. Hallock, 2013: Current and hydrographic conditions at the East Flower Bank in 2011. *Cont. Shelf Res.,* **63,** 43–58.

Terray, E. A., M. A. Donelan, Y. C. Agrawal, W. M. Drennan, K. K. Kahma, A. J. Williams III, P. A. Hwang, and S. A. Kitaigorodskii, 1996: Estimates of kinetic energy dissipation under breaking waves. *J. Phys. Oceanogr.,* **26,** 792–807.

Thorpe, S. A., 2004: Langmuir circulation. *Annu. Rev. Fluid Mech.,* **36,** 55–79.

——, 2005: *The Turbulent Ocean*. Cambridge University Press, 439 pp.

Tseng, R.-S., and E. A. D'Asaro, 2004: Measurements of turbulent vertical kinetic energy in the ocean mixed layer from Lagrangian floats. *J. Phys. Oceanogr.,* **34,** 1984–1990.

Webb, A., and B. Fox-Kemper, 2011: Wave spectral moments and Stokes drift estimation. *Ocean Modell.,* **40,** 273–288.

Weller, R. A., and J. F. Price, 1988: Langmuir circulation within the oceanic mixed layer. *Deep-Sea Res.,* **35,** 711–747.

Zedel, L., and D. Farmer, 1991: Organized structures in subsurface bubble clouds—Langmuir circulation in the open ocean. *J. Geophys. Res.,* **96** (C5), 8889–8900.